

Chasing Snowstorms: The Investigation of Microphysics and Precipitation for Atlantic Coast-Threatening Snowstorms (IMPACTS) Campaign

Lynn A. McMurdie¹, Gerald M. Heymsfield², John E. Yorks², Scott A. Braun², Gail
Skofronick-Jackson³, Robert M. Rauber⁴, Sandra Yuter⁵, Brian Colle⁶, Greg M.
McFarquhar⁷, Michael Poellot⁸, David R. Novak⁹, Timothy J. Lang¹⁰, Rachael Kroodsma^{2, 11},
Matt McLinden², Mariko Oue⁶, Pavlos Kollias⁶, Matthew R. Kumjian¹², Steven J.
Greybush¹², Andrew J. Heymsfield¹³, Joseph A. Finlon¹, Victoria L. McDonald¹, Stephen
Nicholls¹⁴

¹*Department of Atmospheric Sciences, University of Washington, Seattle, WA*

²*NASA Goddard Space Flight Center, Greenbelt, MD*

³*NASA Headquarters, Earth Sciences Division*

⁴*Department of Atmospheric Sciences, University of Illinois at Urbana-Champaign, Urbana,
IL*

⁵*Department of Marine, Earth and Atmospheric Sciences, North Carolina State University,
Raleigh, NC*

⁶*Division of Atmospheric Sciences, State University of New York, Stony Brook, NY*

⁷*Cooperative Institute for Severe and High Impact Weather Research and Operations and
School of Meteorology, University of Oklahoma, Norman, OK*

⁸*Department of Atmospheric Sciences, University of North Dakota, Grand Forks, ND*

⁹*Weather Prediction Center, NOAA/NWS/NCEP, College Park, MD*

¹⁰*NASA Marshall Space Flight Center, Huntsville, AL*

¹¹*Earth System Science Interdisciplinary Center, University of Maryland, College Park, MD*

¹²*Department of Meteorology and Atmospheric Science, The Pennsylvania State University,
University Park, PA*

¹³*National Center for Atmospheric Research, Boulder, CO*

¹⁴*Science Systems and Applications, Inc., Lanham, MD*

Submitted to the Bulletin of the American Meteorological Society

Revised 8 December 2021

Corresponding Author: Lynn A. McMurdie, Department of Atmospheric Sciences,
University of Washington, Box 351640, Seattle, WA 98195, lynnm@uw.edu

ABSTRACT

The Investigation of Microphysics and Precipitation for Atlantic Coast-Threatening Snowstorms (IMPACTS) is a NASA-sponsored field campaign to study wintertime snowstorms focusing on East Coast cyclones. This large cooperative effort takes place during the winters of 2020 – 2023 to study precipitation variability in winter cyclones to improve remote sensing and numerical forecasts of snowfall. Snowfall within these storms is frequently organized in banded structures on multiple scales. The causes for the occurrence and evolution of a wide spectrum of snowbands remain poorly understood. The goals of IMPACTS are to characterize the spatial and temporal scales and structures of snowbands, understand their dynamical, thermodynamical and microphysical processes, and apply this understanding to improve remote sensing and modeling of snowfall. The first deployment took place in January – February 2020 with two aircraft that flew coordinated flight patterns and sampled a range of storms from the Midwest to the East Coast. The satellite-simulating

ER-2 aircraft flew above the clouds and carried a suite of remote sensing instruments including cloud and precipitation radars, lidar, and passive microwave radiometers. The in-situ P-3 aircraft flew within the clouds and sampled environmental and microphysical quantities. Ground-based radar measurements from the National Weather Service network and a suite of radars located on Long Island, NY, along with supplemental soundings and the New York State mesonet ground network provided environmental context for the airborne observations. Future deployments will occur during the 2022 and 2023 winters. The coordination between remote sensing and in situ platforms makes this a unique publicly-available dataset applicable to a wide variety of interests.

CAPSULE

IMPACTS is a multi-year, comprehensive field campaign collecting remote and in-situ cloud and precipitation measurements to study snowfall in North American East Coast winter cyclones.

BODY of ARTICLE

Winter snowstorms impact large populations, affecting as many as 100 million people in major urban corridors along the eastern seaboard of the United States (US), and covering over one million sq kilometers (or 400,000 sq miles; Kocin and Uccellini 2004). Snowy conditions contribute to flight cancellations, power grid outages, school and business closings, and a multitude of vehicle crashes, injuries and fatalities annually in the US, primarily in the Northeast and Midwest (Black and Mote 2015; Guarino and Firestine 2010; Hines and Talukdar 2009; Pisano et al. 2008). Economic impacts on individual states can be as much as \$300 - \$700 million per snow-shutdown day (HIS Global Insight 2014). The

mesoscale variability in precipitation type, snowfall rates, and amounts presents a major challenge to operational forecasters (Nicosia and Grumm 1999; Kocin and Uccellini 2004). Substantial errors in forecasts of precipitation type and quantity can result from relatively small errors (~100-200 km) of the forecast rain-snow line, small forecast errors of the location of bands of higher intensity snowfall, or inadequate characterization of the microphysical growth regimes within numerical models (Zhang et al. 2002; Ganetis and Colle 2015; Greybush et al. 2017; Connelly and Colle 2019; Radford et al. 2019). Improving the understanding of snowfall processes and prediction of snowfall amounts, intensity, timing and distribution will have broad societal and economic benefits.

Snowfall totals can range from a few mm to up to a meter over a relatively short distance during a single storm event, even in the absence of strong terrain influences (e.g., Picca et al. 2014). Figure 1 demonstrates this strong mesoscale variability of snowfall for a storm that occurred 01 – 02 February 2021. The 24-h snowfall totals ranged from less than 0.25 cm (< 0.1 in) over portions of Ohio, western New York, and Pennsylvania to 45 - 60 cm (1.5 - 2 ft) over portions of New York, Connecticut, and Massachusetts. This mesoscale variability in location, type, and intensity of precipitation often results from precipitation banding (e.g., Houze et al. 1976; Matejka et al. 1980; Sanders and Bosart 1985; Wolfsberg et al. 1986; Geerts and Hobbs 1991; Jurewicz and Evans 2004; Novak et al. 2004, 2008, 2010; Griffin et al. 2014; Picca et al. 2014, Ganetis et al. 2018). The processes contributing to the observed precipitation banding in winter cyclones vary widely on temporal and spatial scales. The larger-scale, or primary, bands are most likely associated with mid-level frontogenesis processes (e.g., Novak et al. 2004, 2008), and have been associated with a spectrum of instabilities, such as conditional symmetric instability (e.g., Schultz and Schumacher 1999), conditional instability (e.g., Trapp et al. 2001; Morales 2008) and inertial instability (e.g., Jurewicz and Evans 2004; Schultz and Knox 2007). Ganetis et al. (2018) showed that sets of

roughly parallel mesoscale bands occurred in a wide range of frontogenesis and moist potential vorticity environments. Possible mechanisms associated with mesoscale multi-banded structures include elevated convection, generating cells, shear instabilities, and gravity wave activity (Bosart and Sanders 1986; Zhang et al. 2001, 2003; Kumjian et al. 2014; Plummer et al. 2014, 2015; Rauber et al. 2014, 2017; Rosenow et al. 2014, 2018; Keeler et al. 2016a, b, 2017; Lackmann and Thompson 2019), as illustrated in Figure 2. Numerical models often fail to realistically predict the spectrum of snowbands in winter storms, possibly because of incomplete representations of snow growth processes and wind deformation fields (Connelly and Colle 2019; Harrington et al. 2013a,b; Jensen et al. 2017). Major aspects of snowbands at all scales remain poorly understood, such as how bands are initiated and organized; how the vertical variability of horizontal and vertical motions and thermodynamic instabilities translate to increased snowfall rates at the surface; and how the environmental and microphysical properties vary within and outside of snowbands.

Many regions across the globe lack direct measurements of precipitation or adequate radar coverage. Their remote locations (e.g., mountainous, oceanic, or polar regions) make surface measurements of precipitation difficult or impossible. These limitations highlight the importance of satellite-based global precipitation data especially for monitoring and predicting precipitation distribution in winter cyclones. The current NASA Global Precipitation Measurement (GPM) mission (Hou et al. 2014; Skofronick-Jackson et al. 2017) includes a state-of-the-art Core Observatory flying at an inclined non sun synchronous orbit equipped with the first space-borne multiple-frequency radar, the Dual-Frequency Precipitation Radar (DPR), and a multi-frequency passive microwave radiometer, the GPM Microwave Imager (GMI). The 2017-2027 Decadal Survey for Earth Science and Applications from Space (NASEM 2018) calls for a future mission with radars and multi-frequency passive microwave and sub-mm radiometers, which led to the recent development

of the NASA Earth System Observatory (ESO) Atmosphere Observing System (AOS) mission to address science goals related to clouds, convection, and precipitation. Although a key GPM objective is to detect and measure falling snow at the surface over a wide range of snowfall intensities, the current GPM algorithms are limited by rather large uncertainties in snow amounts (Skofronick-Jackson et al. 2017). Challenges facing remote sensing of snow include, among others, attenuation, scattering from complex particle geometries, variations in particle densities, partially melted and mixed-phase particles, and presence of supercooled liquid water. To address these challenges and improve retrievals for future missions such as ESO/AOS, concurrent measurements by remote-sensing instruments at the same frequencies of space-borne instruments, such as the DPR and GMI, together with in-situ microphysical measurements of particle geometries and intrinsic properties (e.g., ice water content, cloud liquid water) and environmental variables are necessary.

The Investigation of Microphysics and Precipitation of Atlantic Coast-Threatening Snowstorms (IMPACTS) is a current NASA Earth Venture-Suborbital-3 (EVS-3) field campaign to improve the understanding of snowfall processes, remote sensing of snow, and the prediction of banded structure and evolution. It is the first major field study to focus on precipitation processes in winter storms along the US East Coast in over 30 years (e.g., see Dirks et al. 1988 and Hadlock and Kreitzberg 1988 for description of the earlier campaigns). IMPACTS takes place over three winter seasons, with the first deployment completed during January – February 2020. Two additional deployments are planned for winters 2022 and 2023. IMPACTS science objectives as illustrated in Figure 3 are to 1) characterize the spatial and temporal scales of snowband structures in winter storms; 2) understand the dynamical, thermodynamical, and microphysical process that produce snowband structures, and 3) apply this understanding of the structures and underlying processes to improve remote sensing and modeling of snowfall. IMPACTS is designed to achieve these goals through coordinated

flights using aircraft equipped with instruments ideally suited to study mixed-phase clouds, augmented with ground-based radar, rawinsonde and surface observations, data from multiple NASA and NOAA satellites, and regional analyses and convection-permitting short-term forecasts.

IMPACTS Observational Strategy

The primary observing platforms for IMPACTS are two instrumented aircraft that observe storms of interest: the “satellite-simulating” ER-2, which flies high above the storms equipped with passive and active remote-sensing instruments at the same or similar frequencies as instruments flown on precipitation measuring satellites; and the “cloud-penetrating” P-3, which flies within clouds equipped with microphysical probes and environmental measuring instrumentation. The combination of remote sensing observations that provide detailed horizontal and vertical measurements of precipitation structures and co-located microphysical measurements addresses IMPACTS goals to characterize and understand snowband structure and apply this understanding to improving remote sensing and modeling. Due to the long flight duration capabilities of each aircraft, IMPACTS is able to sample snow storms over a large geographical region, spanning from the Midwest to the East Coast, as illustrated in Figure 4 for the winter 2020 deployment season. This allows a variety of storms to be sampled, does not limit operations to a small area due to dependence on ground instruments deployed in one location, and allows for observations of snow outside the East Coast if snow conditions are infrequent along the coastal region in a season, as was sometimes the case in 2020.

The ER-2 serves as an advanced cloud and precipitation remote-sensing platform capable of simulating satellite sensors, but with a much higher spatial and temporal resolution. By using an aircraft platform, sampling across snowband structures multiple times in the same storm is possible and is not limited to when a satellite passes over a storm. The

instrumentation includes multiple-frequency Doppler radars (W, Ka, Ku, and X band) and passive microwave radiometers at a range of frequencies, a cloud lidar and a lightning sensor array (see Table 1 for the list of instruments deployed during the 2020 winter season). The range of radar frequencies provides high sensitivity to cloud tops and light snowfall (W and Ka bands) and relative insensitivity to attenuation in heavy snowfall (Ku and X bands). The nadir sampling by the radars provides high vertical resolution of the cloud systems, and the Doppler capabilities of all the radars allow the ability to detect vertical motions across the storms both within and outside of snowbands. The microwave radiometers provide horizontal sampling and span a range of frequencies for measuring rain and snowfall over land and water. Horizontal winds can be retrieved utilizing the conically-scanning ability of the X-band radar for 2D winds (e.g., Helms et al. 2020) and 3D winds (Guimond et al. 2014). The lidar provides the highest possible sensitivity to thin clouds and enables detection of supercooled liquid water in generating cells near cloud tops (McGill et al. 2004). Airborne radar, radiometer, and lidar observations can be used in various retrievals to provide particle size and other microphysical information (e.g., Grecu et al. 2018; Chase et al. 2018; Mitrescu et al. 2005). The Lightning Instrument Package (LIP) measures the electric field and changes due to lightning occurrence (Schultz et al. 2021).

The P-3 serves as an in-situ platform for sampling microphysical particle characteristics, the local environment of the particles, and the vertical thermodynamic and kinematic profiles from dropsondes (see Table 2 for the list of instruments and their characteristics for the 2020 Deployment). Multiple probes measure microphysical properties such as liquid water content, total water content, particle size and shape, and the presence of supercooled liquid water across a wide range of particle sizes, from small cloud particles (2 μm) to large crystal aggregates (10 cm). The Turbulent Air Motion Measurement System (TAMMS) gives the high-resolution flight-level 3D-wind field, temperature, and humidity,

and when flights are over open ocean, dropsondes are launched to obtain vertical profiles of pressure, temperature, relative humidity, and winds. These in-situ measurements provide critical cloud and snowband structure information, and, when combined with the remote-sensing information from the ER-2 instrument suite, data from the operational NWS Weather Surveillance Radar 1988-Doppler (WSR-88D) radar network, ground-based remote and meteorological sensors, and special rawinsondes, provide measurements critical for improving satellite snowfall retrieval algorithms.

The two aircraft fly in approximately vertically stacked, coordinated patterns (Figure 5) with flight legs generally orthogonal to the snowband orientation. The P-3 samples at different altitudes to capture the vertical structure and temperature dependence of microphysical properties, from which information about microphysical processes, such as rapid crystal growth by vapor deposition (-10 to -20°C; Rogers and Yau 1989), peaks in aggregation efficiency (-12.5 to -17°C and -4 to -6°C; Mitchell 1988; McFarquhar et al. 2007) and secondary ice production processes (< -10°C; Field et al. 2017) can be inferred. The warmer temperature ranges (~ -5°C) may at times be below the minimum flight altitude for the P-3 (roughly 1.5 km, varying regionally over land), so may not always be sampled. Ice nucleation often occurs at much colder temperatures that are typically above the maximum flight altitude of the P-3 (7 – 8.5 km depending on fuel load), so is not a focus for IMPACTS. The ER-2 cruise speed is approximately 205 m s⁻¹ and the P-3 speed ranges between 140 to 160 m s⁻¹ depending on altitude. Because the aircraft cruise speed differs, the ER-2 flight legs are longer than the P-3's to compensate. The legs are timed so that the aircraft are vertically aligned at the center of each flight track and the time difference between the two aircraft at the end of the legs is no more than 5 minutes. This space/time differential at the end of the flight legs can introduce some uncertainty relating the microphysical properties to radar measurements especially for the small-scale features, but is

within minimum distance and time criteria used in previous studies (Heymsfield et al. 2016; Chase et al. 2018; Finlon et al. 2019; Ding et al. 2020; Duffy et al. 2021). The typical flight patterns during IMPACTS primarily consist of a single repeated track, a racetrack, or lawn-mower type patterns depending on storm movement and available flight corridors (Fig. 4).

Although IMPACTS is primarily an aircraft-based field campaign, ground-based observing networks augment the aircraft observations and are critical to achieve IMPACTS goals (Figure 3). By focusing on the Northeast and Midwest US, IMPACTS takes advantage of the NOAA observing infrastructure including the rawinsonde network, National Weather Service (NWS) Automated Surface Observing System (ASOS) surface meteorological stations, and the WSR-88D radar sites. These radars provide large-scale context on the horizontal structure and movement of snowbands, but lack the vertical resolution necessary to diagnose the range of processes that may be contributing to snowband formation, evolution, and structure; thus, the need for aircraft observations. Vertical profiles of temperature, humidity, and winds from rawinsonde launches provide the environmental context of snowband structure. During IMPACTS operations, additional rawinsonde launches up to 3-hourly frequency are launched at NWS rawinsonde operational sites near the planned aircraft flight tracks. In addition, 2 – 3 mobile sounding teams launch soundings at locations determined by the flight-planning mission scientists. Locations used during the 2020 deployment were at Stony Brook, Long Island, University of Illinois at Urbana-Champaign, and Binghamton, New York (Figure 4). The Binghamton, NY, team traveled to multiple locations throughout the Northeast US during 2020, whereas the Stony Brook team remained on Long Island (see Sidebar 1). Both teams, and a team from Millersville University, will be fully mobile in 2022 and 2023.

When storms of interest occur near Long Island, NY, the well-instrumented ground site at Stony Brook University (SBU) contributes important observations of snowbands

250 (<https://you.stonybrook.edu/radar/>). This facility includes multiple radars, profiling
251 microwave radiometers, a scanning Doppler Lidar, and Parsivel disdrometers (see Table 3).
252 The X-band, phased-array radar (SKYLER) is mounted on a mobile truck and can be
253 positioned strategically to sample storms of interest. During the 2020 deployment, SKYLER
254 remained on Long Island, but in subsequent deployments, this facility will deploy to other
255 locations within a 300-km radius of SBU to better sample storms where they occur.

256 In addition to the ASOS NWS surface observations of standard meteorological
257 variables, data from the New York State mesonet observing network are also part of the
258 IMPACTS observing strategy (Brotzge et al. 2020). The NY mesonet consists of 126 surface
259 weather stations (standard meteorological variables, gauge measurements of the liquid
260 equivalent of falling precipitation, and snow depth) and 17 sites with profiling lidars (up to 3
261 km) and microwave radiometers (temperature and humidity up to 10 km). In addition, 20
262 surface sites provide snow liquid equivalent measurements. More information about the NY
263 mesonet is given at (<http://www.nysmesonet.org>) and Brotzge et al. (2020).

264 High-resolution numerical modeling is integral to IMPACTS, both in terms of
265 forecast support for operations and for addressing the science goals. During the 2020
266 deployment year, high-resolution regional model runs with varying initial conditions focused
267 on the Northeast US were run by SBU and the NWS in real time to support operational
268 decisions. During the data analysis phase, model runs will first be evaluated against the
269 observed thermodynamic profiles and precipitation structures from radar, including dual-pol
270 radar estimates of hydrometeor type, and inferred regions of aggregation and riming within
271 the cloud. Then, model microphysics schemes will be evaluated and compared to
272 measurements by the P-3 microphysical probes such as ice water content and derived
273 quantities as well as compared to ground-based estimates of the fallspeeds, size distributions,
274 habit type, and degree of riming, using the ground instruments at SBU (see Table 3). The

Penn State WRF Ensemble Kalman Filter (EnKF) modeling and data assimilation system (e.g., Zhang et al., 2009; 2019) will be used to assimilate conventional observations, satellite observations, and IMPACTS airborne observations (both remotely sensed and in-situ meteorological variables) to produce high-resolution 4D integrated analyses of storms. These analyses synthesize the observations across multiple observing platforms, and are being used to investigate the structure and evolution of multiscale bands and their associated dynamical, thermodynamical, and microphysical processes. The ensemble data assimilation system will also be used for targeted parameter estimation studies (e.g., Nystrom et al., 2021), which will quantify the optimum values for snow growth parameters in the bulk microphysics schemes, as well as quantify their uncertainty, with the rich in-situ microphysics probe data used for evaluation. In addition to advancing the science investigations of IMPACTS, simulations and analyses can provide insights for optimal design of data assimilation, modeling, and ensemble prediction systems for these impactful winter storms.

Successful Project Coordination: The 2020 Deployment Year

IMPACTS operations require careful coordination between forecasting, Air Traffic Control (ATC), decision making, aircraft flight tracks, and scheduling of ground assets. The 2020 deployment year successfully executed this coordination. When a storm of interest was forecast, the IMPACTS mission scientists designed flight tracks for the P-3 and ER-2 aircraft that were submitted 48 h in advance to the ATC agencies overseeing the airspace of interest for approval. The IMPACTS team coordinated with the NWS to discuss the forecast situation and schedule additional sounding launches (usually at 3-hourly intervals) at operational sites bracketing the planned flight time periods, and the mobile IMPACTS sounding teams were deployed to locations pertinent to the planned event. In addition, the NWS requested a GOES-E mesoscale sector for the time period and geographical region of interest to obtain high spatial and temporal resolution GOES-E imagery over the developing storm. If the

storm of interest was in the vicinity of the Stony Brook radar site, the radars operated during the storm bracketing the planned flight period, with the mobile SKYLER radar positioned strategically at one of the pre-planned sites on Long Island, NY. During flight operations, adjustments to the planned flight legs were made in coordination with ATC in real time as warranted based on the observed temperature profiles and observed satellite and radar features to meet the IMPACTS science goals.

The 2020 IMPACTS deployment occurred from 10 January to 29 February 2020. A Field Catalog where all quick-look imagery of the data collected, science and mission reports for all flights, supporting meteorological maps, and tools for exploring each event is available at http://catalog.eol.ucar.edu/impacts_2020. The quality-controlled data for the 2020 deployment can be obtained from the Global Hydrometeorology Resource Center site for IMPACTS (McMurdie et al. 2019).

The 2020 deployment year was uncharacteristically warm along the eastern seaboard and the number of snow events was lower than typical for the region (NCEI 2020). Ten storms were sampled by aircraft (Table 4) that included two Midwest snowstorms, and a few warmer events with primarily rain at the surface. Of these storms, five storms had full coordination between the two aircraft. Figure 4 shows where the sampling took place for all the events. In the following sections, example results from the 2020 deployment highlight each of the different observing platforms and how these types of measurements address IMPACTS goals.

Preliminary Results: Characterizing and Understanding Snowbands

Complementary measurements obtained from the ER-2 airborne radars and the P-3 in-situ microphysical instruments, and how together they address the IMPACTS goals of characterizing and understanding snowbands is illustrated in Figures 6 and 7 for the 7 February 2020 event. At this time, a rapidly deepening surface cyclone was located over

eastern Pennsylvania and the aircraft made several west-to-east transects across precipitating clouds to the north over central New York State. Figure 6 relates the radar reflectivity from the 0.9° elevation angle scan of the KENX WSR-88D radar in Albany, NY, to the ER-2 X-band radar (EXRAD) nadir-pointing radar reflectivity cross-section as the aircraft transected overhead. Although the region of highest reflectivity (greater than 40 dBZ at ~43°N 74.5°W) shown in Fig. 6a is associated with the bright band (where melting snow produces high reflectivity), snow was falling at the surface to the region west of 74.5°W, as measured by the New York Mesonet stations (Fig. 8).

The WSR-88D radar beam intersected the P-3 flight track at 1558 UTC and both the EXRAD and WSR-88D indicated an area of enhanced reflectivity of ~28 dBZ (magenta box in Figure 6b) that is part of a snowband-like structure circled in magenta in Fig. 6a. To examine whether processes such as locally stronger upward vertical velocity is contributing to this snowband-like structure, a Contoured Frequency by Altitude Diagram (CFAD, Yuter and Houze 1995) of radial velocity measurements from the nadir pointing radars on the ER-2 (e.g., HIWRAP Ka-band radar, Fig. 6c) is used to estimate the magnitude of the vertical motion. The black contour in Fig. 6c is the median radial velocity at each altitude bin and represents the particle ensemble fall speed profile that's added to the measured HIWRAP Ka-band radial velocity to obtain an estimate of the vertical velocity following Rosenow et al. (2014). The resulting estimated vertical motion field shows that the region of interest of enhanced reflectivity at 1558 UTC near 75.5°W was also associated with a local region of upward vertical motion ~ 0.5 m/s (magenta box Fig. 6d).

The reflectivity profile measured by the other ER-2 radars (W, Ka-band, and Ku-band) along with microphysical properties measured by the P-3 focusing on the same region of the snowband-like structure discussed above is shown in Fig. 7. The dual-frequency ratio, defined as the ratio of radar reflectivity factor between two wavelengths (DFR_{Ku-Ka}), is

plotted in the bottom panel of Fig. 7a. Past studies have shown that spatial variability in DFR is influenced by variations in microphysical properties (e.g. Matrosov et al. 2005; Liao et al. 2016; Mason et al. 2019), and the coordinated flight legs between the ER-2 and P-3 performed in IMPACTS allows further exploration of the microphysical properties that cause variations in DFR in winter cyclones. The region of enhanced DFR coincides with an increase in the mean diameter of the sampled particles (i.e. larger mass-weighted mean particle diameter, D_m , Fig. 7b) and an increased number of larger particles per unit volume (highlighted with red boxes in Fig. 7) compared to the other times. Figure 7c illustrates that a significant number of large aggregates were sampled during that time. Later near 1600 UTC (blue boxes in Figure 7), the reflectivity at all radar wavelengths was lower than before, the D_m decreased, the concentration of larger particles decreased, and aggregation was less prevalent. Additional particle imagery obtained from the PHIPS instrument from this case during other flight legs is highlighted in sidebar 2.

In this one example flight leg of the 7 February 2020 event, the snowband-like structure was characterized by locally enhanced reflectivity in the NEXRAD and ER-2 radars (magenta and red boxes in Figs. 6 and 7) and upward vertical motion which may have contributed to the increased aggregation and larger particle sizes as measured by the P-3. This example illustrates how measurements from multi-frequency radars and in situ microphysics measurements together illuminate processes present in snowbands. More in depth analysis of this event is ongoing addressing IMPACTS goals, such as how the vertical variability of horizontal and vertical motions translated to increased snowfall rates in central New York and how the environmental and microphysical properties varied within and outside the regions of heavier snowfall.

Another example of how the IMPACTS observations provided a synergistic view of the mesoscale processes in winter storms is illustrated with the last storm sampled during the

2020 deployment year on 27 February 2020. A mature, deep occluded cyclone was situated over northern New York, and the ER-2 sampled the region to the west of an occluded front located from Lake Ontario to Long Island, NY. During the 0954 – 1005 UTC 27 February flight leg, there were wave-like features to the west of the leg evident in the 1000 UTC GOES-16 IR imagery (Figure 9, 43°N 78°W). The ER-2 sampled the region immediately west of the occluded front in the cold sector and also along a convergence zone on the western edge of an 850-hPa jet situated over northeastern New York State (not shown). Variability in cloud top height or wave-like features are not obviously present along this flight track in the GOES imagery (Fig. 9). However, the 1064-nm total attenuated backscatter from the Cloud Physics Lidar (CPL; McGill et al., 2002) and the W-band (94-GHz) CRS radar reflectivity data from the ER-2 tell a different story (Figure 10a and b). Both CPL and CRS serve complimentary roles in IMPACTS due to their respective strengths and weaknesses. CPL can measure optically thin cloud tops and non-precipitating cloud particles below CRS's minimum detection threshold (-28 dBZ), whereas CRS provides extensive hydrometer particle information below where CPL fully attenuates (cloud optical depth of ~3.0). CRS shows the nearly ubiquitous presence of tilted fall streaks of varying intensity throughout the flight line. Model and rawinsonde data (not shown) indicate enhanced speed and direction shear, especially in regions where the tilted fall streaks are most pronounced (~3-4 km above sea level, ~9:56 UTC), which is near and just above the height of the frontal inversion. Despite these insights from CRS, its lower sensitivity limits its application near cloud top where CPL detected an extensive layer of optically thin clouds. Thus, CRS echo tops heights were up to 1 km lower than detected by CPL (~0955 UTC).

CPL and CRS data limitations however motivate both this and previous studies (i.e., McGill et al., 2004; Delanoe and Hogan, 2010; Mace and Zhang, 2014) to develop combined lidar-radar data products to provide a holistic view of the hydrometer and storm vertical

structure. The combined CRS-CPL data product shown in Figure 10c shows the maximum normalized signal (CRS = reflectivity, CPL = backscatter) derived from both data products. Normalization was achieved by differencing all grid points from their dataset minimum and then dividing this difference by an empirically derived range of values observed for each instrument during the IMPACTS 2020 field campaign. In Figure 10c, values range between 0 (weak return signal) and 1 (strong return signal) with regions of overlap denoted with stippling. These data show that the wave-like or fall streak pattern evident in CRS data was most likely obscured from GOES (Figure 9) due to optical thin clouds further aloft and also affords a more comprehensive visualization of the fall streaks than either CPL or CRS could provide independently. Additionally, IMPACTS affords the unique opportunity to develop and test combined lidar (Yorks et al. 2011; Midzak et al. 2020) and radar (Oue et al. 2015) data products to enable pseudo-microphysical retrievals. Such retrievals would provide information about particle shape and phase from cloud top to the surface, which can be evaluated with the IMPACTS suite of in-situ cloud particle measurements. Preliminary results using normalized combined CRS-CPL depolarization data (not shown) suggest that particle phase changes often mirrored the wave-like patterns seen in Figure 10c. Visualizing and analyzing both storm structure and its underlying microphysical characteristics via merged data products, in the context of model, space, and airborne data, affords the unique opportunity to investigate how these wave-like patterns form, their microphysical characteristics, and their potential role in forming and maintaining snow bands.

Research quality ground-based radars installed at SBU (Table 3) are critical for characterizing the short time scale evolution of snowband structures and associated mechanisms contributing to snow band maintenance which cannot be addressed by the aircraft sampling. Figure 11 highlights the ground observations made as a warm frontal snow band located in the prefrontal sector north of the surface warm front crossed over Long Island

and southern New England on 18-19 January 2020. The WSR-88D KOKX radar observed a NNW-SSE oriented primary snowband passing through SBU near 1900 UTC 18 January 2020 (Figure 11a). The SBU radars allow the exploration of snowband mechanisms for this event. Vertical and quasi-vertical profiles (Ryzhkov et al. 2016; Kumjian and Lombardo 2017) from radars at SBU all show a rapid onset of snowfall to the surface around this time, as the dry low-level air ahead of the band retreated (Figure 11b-d). There were fall streaks from convective cells aloft that had higher reflectivities towards the ground in the W-band (ROGER) and MRR reflectivity fields (Figure 11b, d), but the band was also located within a layer of frontogenesis from 900 - 850 hPa and associated with upward motion (not shown). The KASPR radar has fully polarimetric capabilities and operated in Range Height Indicator mode, sampling across the band as it moved across Long Island. Movies of reflectivity, spectrum width and specific differential phase (K_{DP}) from the KASPR radar for more than a 2- hr period as the band moved across Long Island are provided as supplemental material (supplement 1). Multiple layers of turbulence below 4 km AGL were inferred from the spectrum width measurements as the band moved across Long Island. These turbulent motions could have provided a mechanism for aggregation and additional particle mass growth by riming. Multi-scale processes such as vertical motions associated with frontogenesis and turbulent motions all appear to have contributed to the snowfall mechanisms associated with this case. Ongoing analysis of this event and others where the ground-based radar observations can be related to the airborne remote sensing and in situ observations will provide considerable insights to the processes contributing to banded structures.

Preliminary Results: Applying IMPACTS Observations to Remote Sensing

The IMPACTS observational strategy of coincident remote sensing and in situ microphysical measurements in precipitating winter cyclones is especially beneficial when

450 they align along a GPM satellite overpass, such as the 1 February 2020 event when the
451 aircraft lined up under a 1435 UTC GPM overpass over the Atlantic Ocean. Figure 12 shows
452 the visible satellite image of the cloud field associated with a developing surface low off the
453 North Carolina coast on 1 February 2020 with the GPM overpass and the ER-2 flight track
454 overlaid. Although this event was warm and produced rain at the surface, the measurements
455 obtained by IMPACTS address the science goal to improve remote sensing of precipitation.
456 The ER-2 flew over several fine-scale west-east oriented linear bands of thicker clouds
457 between 36° and 37°N . The reflectivity field from the HIWRAP Ku-band radar in Figure 13a
458 illustrates that these bands were tall convective turrets extending to over 8 km above sea
459 level, about 3 km above the top of the broader cloud deck. The reflectivity was also enhanced
460 along the bright band under these turrets (especially at 35.9° , 36.4° and 37.2°N) compared to
461 other locations, and there appears to be heavy precipitation reaching the surface beneath these
462 regions. The GPM DPR Ku-band reflectivity plotted in Figure 13b also confirms the presence
463 of narrow and tall convective turrets and enhanced reflectivity at the bright band and below at
464 the same locations listed above. The DPR has coarser resolution than HIWRAP and shows
465 evidence of significant non-uniform beam filling. The P-3 flew underneath the ER-2 at 5 km
466 elevation and sampled the tops of the lower cloud deck and within the convective turrets.
467 Figure S2 in Sidebar 2 shows some sample particle imagery from the PHIPS and CPI during
468 this transect. When the P-3 was sampling the top of the lower cloud deck ($\sim 36.125^{\circ}\text{N}$ in Fig.
469 13), the temperature was -10°C and all the particles were supercooled liquid drops (See first
470 image in Fig. S2). Then when the P-3 entered the convective turret at 36.25°N , the cloud
471 particles were predominantly ice and included capped columns and plate aggregates (see
472 imagery highlighted within the purple box in Fig. S2). This example shows the rich variations
473 in the precipitation structures detected from the airborne instrumentation that can then be

applied to the evaluation and future development of satellite retrievals of microphysical properties and rain rate.

The ER-2 also flew two microwave radiometers, AMPR and CoSMIR (Table 1). AMPR's frequencies make up much of the lower end of the GPM Microwave Imager (GMI), whereas the CoSMIR frequencies span the upper end of GMI and include frequencies that are sensitive to both rain and snowfall. This airborne passive-microwave observing suite's role in IMPACTS is to characterize the horizontal structure of precipitation systems, and to enable combined active-passive retrievals of rain and snowfall similar to the GPM combined algorithm and related approaches (Grecu et al. 2016; Olson et al. 2016). They are also sensitive to particle phase, size, and shape. Thus, these radiometers tie into all three IMPACTS goals: characterize spatial/temporal scales of heavy winter precipitation; understand processes occurring in heavy winter precipitation; and apply this information to improving remote sensing of precipitation.

Figure 14 shows AMPR, CoSMIR, and GMI swaths that observed precipitation during the same GPM overpass illustrated in Figure 13. The southern portion of the leg overflow strong convection (near 36°N 73°W), where high brightness temperatures (~250 K) at 10.7 GHz (Figure 14a) indicate heavy rain. This high brightness temperature (T_b) at 35.9°N corresponds to the leftmost convective turret in Figure 13a and b discussed above. In this same region, the 37.1-GHz and 85.5-GHz channels (Figure 14c and d) showed brightness temperature minima located within broader areas of warm temperatures, the latter associated with emission from liquid cloud and rain (Weinman and Guetter 1977). Local minima of brightness temperatures in these channels are due to scattering of the upwelling radiation by the presence of ice, which was confirmed by the P-3 PHIPS measurements (Fig. S2). The CoSMIR 165.5 and 183.31 ± 7 GHz T_b values were depressed in this region as well (Figure 14e, f), confirming strong scattering by ice, and that ice processes within the cloud

contributed to heavy precipitation (a simple reflectivity-rainfall relationship applied to EXRAD observations suggested rain rates in excess of 50 mm h^{-1} in this core).

The polarization difference (PD), defined as the difference between the vertical- and horizontal-polarized Tb values for CoSMIR 165.5 GHz and the GMI at 166 GHz are shown in Figure 14g, h. The CoSMIR and GMI PDs agree well with minor differences due to instrument characteristics. The CoSMIR 165.5-GHz PD field shows an even more striking correspondence to the convective bands evident in the GOES-16 visible imagery and the HIWRAP reflectivity (Figures 12, 13 and 14g). Gong and Wu (2017) and Gong et al. (2020) demonstrated that PD values tend to be higher ($>5 \text{ K}$) in stratiform and anvil cloud regions due to the prevalence of predominantly horizontally oriented ice. This effect was observed in the weaker precipitation north of 36°N . Within the convection near 36°N , PD values were somewhat less (by 1-2 K), especially in the GMI observations (Fig. 14h). This suggested more randomized ice particle orientations likely associated with the deep convection there (Fig. S2, Gong et al. 2020).

The ice scattering signatures seen in both the AMPR and CoSMIR fields at the 37.1 GHz and higher frequencies and the presence of ice particles confirmed by the P-3 PHIPS instrument (Fig. S2) indicated that the presence of larger and/or higher concentrations of ice particles played a significant role in the overall precipitation formation for this event, particularly for the heaviest precipitation cores.

Looking forward to the next deployments

IMPACTS successfully measured precipitation structures in 10 winter cyclone events in 2020. Preliminary results highlighted here point to the roles of locally enhanced upward vertical motion, aggregation, wave activity and elevated convection in the observed snowband structures in different storms. In-depth analysis of these cases is ongoing (e.g., Chase et al. 2021; Heymsfield et al. 2021; Schultz et al. 2021, Dunnavan et al. 2022; Finlon

et al. 2022), focusing on the dynamical and thermodynamical processes, and microphysical structures occurring within and outside of snowbands. With the success of the 2020 deployment, the IMPACTS team looks forward to two more winter seasons of measurements, currently planned for January – February 2022 and January – February 2023. The two aircraft will carry essentially the same instrument packages as the first deployment with a full set of microphysical probes on the P-3 and active and passive remote sensing instruments on the ER-2. The ground component will remain primarily focused on Long Island, NY, with extensive instrumentation installed there. The SKYLER mobile X-band radar will have the ability to travel in an approximate 300 km radius from Stony Brook enabling the IMPACTS team to strategically deploy this radar and the mobile sounding unit in a broader region for storm systems of interest. An example of the unique ability of the SKYLER radar to sample detailed precipitation structure through high temporal scanning is shown as a movie in the supplemental material. The IMPACTS team is also interested in collaborating with other research groups to expand the ground component of the observing network, especially those with ground-based instrumentation suited for measuring winter cyclones in the Northeast or Midwest regions of the US. Please contact the authors if interested in participating in the IMPACTS 2023 deployment. As the IMPACTS project moves forward, the in situ and remote sensing measurements of precipitation structures and processes will ultimately address long-standing questions regarding processes contributing to the initiation, structure and evolution of snowbands in winter cyclones, improve snowfall retrievals from space-based missions such as GPM, and improve numerical weather prediction model forecasts of snowfall during US snowstorms.

Acknowledgements

This article is dedicated to Drs. Fuqing Zhang and Gail Skofronick-Jackson, whose contributions and enthusiastic support for IMPACTS and other projects have been

instrumental in advancing knowledge of precipitation systems and advancing the state of spaceborne measurements of precipitation. Field campaigns of this size depend on the dedication and support of many individuals and institutions. We thank the support of the NASA Earth Science Division (ESD), Earth-Venture Suborbital Program under the NASA Airborne Science Program and especially M. Martin, and J. Olsen in the Earth System Science Pathfinder Program (ESSP) that manages the Earth-Venture Suborbital Program (EVS-3), B. Tagg of the ESD Airborne Science Program, and J. Kaye and B. Lefer of the ESD Research Program. The National Weather Service (NWS) provided invaluable support throughout the 2020 deployment and plan to continue their integral involvement in future deployments. We especially thank NWS's J. Waldstreicher for scheduling supplemental rawinsonde launches, GOES-16 mesoscale sectors and for connecting our forecasting team with on-duty NWS Eastern Region and Weather Prediction Center forecasters for daily forecasting support. We thank all members of the IMPACTS instrument teams for the important contributions to the mission's success. In addition to the authors of this paper, the following people have leadership roles in IMPACTS. For overall logistics support and management: V. Salazar, Project Manager, and K. Sterns, from the NASA ARC's Earth Science Project Office. Aircraft operations: J. Nystrom, W. Klein, B. Hobbs, F. Becker, M. Cropper, G. Everson, and K. Griffin, and the ER-2 and P-3 pilots, crew and support teams. Aircraft instrument leads, IMPACTS Co-Investigators and mission science operations: I. Adams, D. Doleen, M. Fritts, M. Grecu, S. Guimond, L. Li, M. McGill, M. Miller, J. Munchak, D. Noone, M. Schnaiter, C. Schultz, L. Thornhill, and D. Toohey. Data Management: S. Brodzik, G. Stano. Forecasting: A. DeLaFrance, M. Han, S. Harkema, C. Helms, D. Hueholt, B. Kiel, M. Leonardo, R. Patel, R. Schrom, L. Tomkins, and P. Yeh. P-3 instrument operators: A. Bansemer, K. Sand, G. Sova, C. Robinson, and F. Waitz. Rawinsonde launching teams: T. Zaremba, A. Janiszewski, the students of the UIUC

574 Atmospheric Sciences Department, the SUNY Stony Brook Atmospheric Sciences
575 Department, and the NCSU Sounding Club. University participants are supported for
576 IMPACTS by NASA Grants 80NSSC19K0338 (UW), 80NSSC19K0354 (NCSU),
577 80NSSC19K0452 (PSU), 80NSSC19K0399 (OU), 80NSSC19K0355 (UI), 80NSSC19K0394
578 (SBU), 80NSSC19K0328 (UND), 80NSSC19K1612 (NCAR), 80NSSC20K1876 (NCAR),
579 80NSSC19K0397 (NCAR), and 80NSSC20K0729 (CU).

580 **Data Availability Statement**

581 All IMPACTS quick-look images and mission scientist reports from the 2020
582 Deployment are highlighted in the field catalog at: http://catalog.eol.ucar.edu/impacts_2020
583 and the data can be obtained from the Global Hydrology Resource Center Distributed Active
584 Archive Center at https://ghrc.nsstc.nasa.gov/uso/ds_details/collections/impactsC.html and
585 [McMurdie et al. \(2019\)](#).

586 **Sidebar 1 - Early Career and Student Participation**

587 The IMPACTS project puts a high priority on training the next generation of science
588 leaders by empowering students and early-career professionals to perform critical mission
589 support roles and participate in data collection efforts. Thus, students and early career
590 scientists are key to the success of IMPACTS mission operations and science analysis.
591 Without their expertise, hard work, and enthusiasm, IMPACTS would not be possible. These
592 individuals performed multiple roles during the IMPACTS 2020 deployment, such as (1)
593 performing sounding observations in remote locations, (2) operating ground-based radar
594 systems for coordination with aircraft measurements, and (3) providing twice daily forecast
595 briefings to the entire IMPACTS team. Students and early career scientists also served as
596 members of the ER-2 instrument teams, while others served as onboard P-3 mission scientists
597 and P-3 instrument operators, communicating in real time with the operations center during

flights. Several of these individuals also had leadership roles in the operations center as the lead mission scientists, where they communicated decisions regarding flight tracks to the flight coordinators in real time and enabled each flight mission to achieve the science goals. Examples of the participation by these individuals are shown in Figure S1.

Sidebar 2

There are many challenges to remote sensing retrievals of ice-phase precipitation within winter extratropical cyclones. Radar and passive microwave measurements from space-borne instruments are strongly affected by particle geometry, which includes not only the size-density spectrum of particles, but also the relative concentrations of pristine and aggregate crystals, the aspect ratios and canting angles of the particles, and their degree of riming. To address these uncertainties, IMPACTS measurement strategy includes in-situ measurements from the P-3 of particle geometries/habits and intrinsic bulk microphysical properties (e.g. ice water content, cloud liquid water, supercooled water content) as well as active and passive remote sensing measurements from the ER-2. Examples of the range of particle types measured during the IMPACTS 2020 deployment as sampled by the PHIPS and CPI instruments are shown in Figure S2. The top group of images within the purple box were all collected during the 1 February 2020 event highlighted in Figs. 13 and 14. The first image of supercooled liquid water droplets is from the CPI instrument collected when the P-3 was skimming the tops of the clouds at 5km. The rest in this box were collected when the P-3 entered a convective turret and the particles rapidly transitioned to primarily ice of mostly capped columns and plate aggregates. The middle group of images within the green box were all collected during the 7 February 2020 event highlighted in Figs. 6 and 7. They are arranged so that the left-most image was collected from the west-most portion of the flight leg and the rightmost image was from the eastern portion of the storm sampled by the P-3. They were

623 collected at different temperatures as shown on the figure. These examples are only a small
624 fraction of the range particles sampled during IMPACTS. These measurements will
625 contribute to improving and constraining current and future retrieval algorithms of ice-phase
626 precipitation.

627

628

References

- Abdelmonem, A., E. Järvinen, D. Duft, E. Hirst, S. Vogt, T. Leisner, and M. Schnaiter, 2016: PHIPS–HALO: the airborne Particle Habit Imaging and Polar Scattering probe – Part 1: Design and operation, *Atmos. Meas. Tech.*, **9**, 3131–3144, <https://doi.org/10.5194/amt-9-3131-2016>.
- Amiot, C. G., S. K. Biswas, T. J. Lang, and D. I. Duncan, 2021: Dual-Polarization Deconvolution and Geophysical Retrievals from the Advanced Microwave Precipitation Radiometer during OLYMPEX/RADEX, *J. Atmos. Oceanic Technol.*, **38**, 607–628, <https://doi.org/10.1175/JTECH-D-19-0218.1>.
- Barrick, J. D. W., J. A. Ritter, C. E. Watson, M. W. Wynkoop, J. K. Quinn, and D. R. Norfolk, 1996: Calibration of the NASA Turbulent Air Motion Measurement System. NASA Technical Paper 3610, Langley Research Center, 24 pp, available from <http://citeseerx.ist.psu.edu/viewdoc/download?doi=10.1.1.57.5766&rep=rep1&type=pdf>.
- Black, A. W., and T. L. Mote, 2015: Characteristics of winter-precipitation-related transportation fatalities in the United States. *Wea. Climate Soc.*, **7**, 133–145, <https://doi.org/10.1175/WCAS-D-14-00011.1>.
- Bosart, L. F., and F. Sanders, 1986: Mesoscale Structure in the Megalopolitan Snowstorm of 11–12 February 1983. Part III: A Large-Amplitude Gravity Wave. *J. Atmos. Sci.*, **43**, 924–939, [https://doi.org/10.1175/1520-0469\(1986\)043<0924:MSITMS>2.0.CO;2](https://doi.org/10.1175/1520-0469(1986)043<0924:MSITMS>2.0.CO;2).
- Brotzge, J. A., and 18 co-authors, 2020: A Technical overview of the New York State mesonet standard network. *J. Atmos. Oceanic Technol.*, **37**, 1827–1845, <https://doi.org/10.1175/JTECH-D-19-0220.1>.

Chase, R. J., and Coauthors, 2018: Evaluation of triple-frequency radar retrieval of snowfall properties using coincident airborne in situ observations during OLYMPEX. *Geophys. Res. Lett.*, **45**, 5752-5760, <https://doi.org/10.1029/2018GL077997>.

Chase, R. J., S. W. Nesbitt, G. M. McFarquhar, N. B. Wood, and G. M. Heymsfield, 2022: Direct comparisons between GPM-DPR and CloudSat snowfall retrievals. *J. Atmos. Meteor. Climatol.*, in review.

Claffey, K. J., K. F. Jones, and C.C. Ryerson, 1995: Use and calibration of Rosemount ice detectors for meteorological research. *Atmos. Res.*, **36**, 277-286, [https://doi.org/10.1016/0169-8095\(94\)00042-C](https://doi.org/10.1016/0169-8095(94)00042-C).

Connelly, R., and B. A. Colle, 2019: Validation of snow multibands in the comma head of an extratropical cyclone using a 40-member ensemble. *Wea. Forecasting*, **34**, 1343-1363, <https://doi.org/10.1175/WAF-D-18-0182.1>.

Delanoë, J., and R. J. Hogan, 2010: Combined CloudSat- CALIPSO- MODIS retrievals of the properties of ice clouds, *J. Geophys. Res.*, **115**, D00H29, <https://doi.org/10.1029/2009JD012346>.

Ding, S., G. M. McFarquhar, S. W. Nesbitt, R. J. Chase, M. R. Poellot, and H. Wang, 2020: Dependence of mass-dimensional relationships on median mass diameter. *Atmos.* **11**, 756, <https://doi.org/10.3390/atmos11070756>.

Dirks, R. A., J. P. Kuettner, and J. A. Moore, 1988: Genesis of Atlantic Lows Experiment (GALE): An Overview. *Bull. Amer. Meteor. Soc.*, **69**, 148-160, [https://doi.org/10.1175/1520-0477\(1988\)069<0148:GOALEA>2.0.CO;2](https://doi.org/10.1175/1520-0477(1988)069<0148:GOALEA>2.0.CO;2).

Duffy, G., G. McFarquhar, S. W. Nesbitt, and R. Bennartz, 2021: Demonstration of a consistent relationship between Dual-Frequency Reflectivity and the mass-weighted

mean diameter in measurements of frozen precipitation from GCPEX, OLYMPEX, and MC3E. *J. Atmos. Sci.*, **78**, 2533-2547, <https://doi.org/10.1175/JAS-D-20-0174.1>.

Dunnavan, E. L., J. Carlin, J. Hu, P. Bukovcic, A. Ryzhkov, G. McFarquhar, J. Finlon, S. Matrosov, and D. Delene, 2022: Radar retrieval evaluation and investigation of dendritic growth layer polarimetric signatures in a winter storm. *J. Appl. Meteor. Climatol.*, in review.

Field, P. R., R. P. Lawson, P. R. A. Brown, G. Lloyd, C. Westbrook, D. Moisseev, A. Miltenberger, A. Nenes, A. Blyth, T. Choularton, P. Connolly, J. Buehl, J. Crosier, Z. Cui, C. Dearden, P. DeMott, A. Flossmann, A. Heymsfeld, Y. Huang, H. Kalesse, Z. A. Kanji, A. Korolev, A. Krchgaessner, S. Lasher-Trapp, T. Leisner, G. McFarquhar, V. Phillips, J. Stith, and S. Sullivan, 2017: Secondary Ice Production: Current state of the science and recommendations for the future. *Meteor. Monograph*, **58**, 7.1-7.20, <https://doi.org/10.1175/AMSMONOGRAPHS-D-16-0014.1>.

Friedrich, K., S. Higgins, F. J. Masters, and C. R. Lopez, 2013: Articulating and Stationary PARSIVEL Disdrometer Measurements in Conditions with Strong Winds and Heavy Rainfall. *J. Atmos. Oceanic Technol.*, **30**, 2063-2080, <https://doi.org/10.1175/JTECH-D-12-00254.1>.

Finlon, J. A., G. M. McFarquhar, S. W. Nexbitt, R. M. Rauber, H. Morrison, W. Wu, and P. Zhang, 2019: A Novel approach for characterizing the variability in mass-dimension relationships: Results from MC3E. *Atmos. Chem. Phys.*, **19**, 3621-3643, <https://doi.org/10.5194/acp-19-3621-2019>.

Finlon, J. A., L. A. McMurdie, and R. C. Chase, 2022: (Joe's paper)

Ganetis, S.A. and B.A. Colle, 2015: The Thermodynamic and Microphysical Evolution of an Intense Snowband during the Northeast U.S. Blizzard of 8–9 February 2013. *Mon. Wea. Rev.*, **143**, 4104–4125, <https://doi.org/10.1175/MWR-D-14-00407.1>.

Ganetis, S. A., B. A. Colle, S. E. Yuter, and N. P. Hoban, 2018: Environmental conditions associated with observed snowband structures within northeast US winter storms. *Mon. Wea. Rev.*, **146**, 3675-3690. <https://doi.org/10.1175/MWR-D-18-0054.1>.

Geerts, B., and P. V. Hobbs, 1991: Organization and structure of clouds and precipitation on the mid-Atlantic coast of the United States. Part IV: Retrieval of the thermodynamic and microphysical structures of a frontal rainband from Doppler radar data. *J. Atmos. Sci.*, **48**, 1287-1305, [https://doi.org/10.1175/1520-0469\(1991\)048<1287:OASOCA>2.0.CO;2](https://doi.org/10.1175/1520-0469(1991)048<1287:OASOCA>2.0.CO;2).

Gong, J. and D. L. Wu, 2017: Microphysical properties of frozen particles inferred from Global Precipitation Measurement (GPM) Microwave Imager (GMI) polarimetric measurements, *Atmos. Chem. Phys.*, **17**, 2741-2757, <https://doi.org/10.5194/acp-17-2741-2017>.

Gong J., X. Zeng, D. L. Wu, S. J. Munchak, X. Li, S. Kneifel, D. Ori, L. Liao, and D. Barahona, 2020: Linkage among ice crystal microphysics, mesoscale dynamics, and cloud and precipitation structures revealed by collocated microwave radiometer and multifrequency radar observations, *Atmos. Chem. Phys.*, **20**, 12633-12653, <https://doi.org/10.5194/acp-20-12633-2020>.

Grecu, M., W. S. Olson, S. J. Munchak, S. Ringerud, L. Liao, Z. Haddad, B. L. Kelley, and S. F. McLaughlin, 2016: The GPM combined algorithm, *AMS J. Atmos. Oceanic Technol.*, **33**(10), 2225-2245. <https://doi.org/10.1175/JTECH-D-16-0019.1>.

Grecu, M., L. Tian, G. M. Heymsfield, A. Tokay, W. S. Olson, A. J. Heymsfield, and A. Bansemer, 2018: Momp-parametric methodology to estimate precipitating ice from multiple-frequency radar reflectivity observations. *J. Appl. Meteor. Climatol.*, **57**, 2605-2622. <https://doi.org/10.1175/JAMC-D-18-0036.1>.

Greybush S. J., S. Saslo, and R. Grumm, 2017: Assessing the Ensemble predictability of precipitation forecasts for the January 2015 and 2016 East Coast winter storms. *Wea. Forecasting*, **32**, 1057-1078, <https://doi.org/10.1175/WAF-D-16-0153.1>.

Griffin, E. M., T. J. Schuur, A. V. Ryzhkov, H. D. Reeves, and J. C. Picca, 2014: A Polarimetric and Microphysical Investigation of the Northeast Blizzard of 8–9 February 2013. *Wea. Forecasting*, **29**, 1271–1294, <https://doi.org/10.1175/WAF-D-14-00056.1>.

Guarino, J., and T. Firestone, 2010: Effects of the February 2010 snowstorms on airline performance. U.S. Dept. of Transportation Special Report, Research and Innovative Technology Administration, August 2010, 5 pp, <http://purl.fdlp.gov/GPO/gpo54017>.

Guimond, S. R., L. Tian, G. M. Heymsfield, and S. J. Frasier, 2014: Wind retrieval algorithms for the IWRAP and HIWRAP airborne Doppler radars with applications to hurricanes. *J. Atmos. Oceanic Technol.*, **31**, 1189-1215, <https://doi.org/10.1175/JTECH-D-13-00140.1>.

Hadlock, R., and C. W. Kreitzberg, 1988: The Experiment on Rapidly Intensifying Cyclones over the Atlantic (ERICA) field study: Objectives and plans. *Bull. Amer. Meteor. Soc.*, **69**, 1309-1320, [https://doi.org/10.1175/1520-0477\(1988\)069<1309:TEORIC>2.0.CO;2](https://doi.org/10.1175/1520-0477(1988)069<1309:TEORIC>2.0.CO;2).

Harrington, J. Y., K. Sulia, and H. Morrison, 2013a: A method for adaptive habit prediction in bulk microphysical models. Part I: Theoretical development. *J. Atmos. Sci.*, **70**, 349-364, <https://doi.org/10.1175/JAS-D-12-040.1>.

Harrington, J. Y., K. Sulia, and H. Morrison, 2013b: A method for adaptive habit prediction in bulk microphysical models. Part II: Parcel model corroboration. *J. Atmos. Sci.*, **70**, 365-376, <https://doi.org/10.1175/JAS-D-12-0152.1>.

Helms, C. N., M. L. Walker McLinden, G. M. Heymsfield, and S. R. Guimond, 2020: Reducing errors in velocity-azimuth display (VAD) wind and deformation retrievals from

748 airborne doppler radars in convective environments. *J. Atmos. Oceanic Technol.*, **37**,
 749 2251-2266, <https://doi.org/10.1175/JTECH-D-20-0034.1>.
 750 Herman, R. L., J. Worden, D. Noone, D. Henze, K. Bowman, K. Cady-Pereira, V. H. Payne,
 751 S. S. Kulawik, and D. Fu., 2020: Comparison of optimal estimation HDO/H₂O retrievals
 752 from AIRS with ORACLES measurements. *Atmos. Meas. Tech.*, **13**, 1825–1834,
 753 <https://doi.org/10.5194/amt-13-1825-2020>.
 754 Heymsfield, A. J., S. Y. Matrosov, and N. B. Wood, 2016: Toward improving ice water
 755 content and snow-rate retrievals from radars. Part I: X and W bands, Emphasizing
 756 CloudSat. *J. Appl. Meteor. Climatol.*, **55**, 2063-2090, [https://doi.org/10.1175/JAMC-D-](https://doi.org/10.1175/JAMC-D-15-0290.1)
 757 15-0290.1.
 758 Heymsfield, A. J., A. Bansemer, A. Theis, and C. Schmitt, 2021: Survival of Snow in the
 759 Melting Layer: Relative Humidity Influence. *J. Atmos. Sci.*, **78**, 1823-1845,
 760 <https://doi.org/10.1175/JAS-D-20-0353.1>.
 761 Hines, P., J. Apt, and S. Talukdar, 2009: Large blackouts in North America: Historical trends
 762 and policy implications. *Energy Policy*, **37**, 5249-5259,
 763 <https://doi.org/10.1016/j.enpol.2009.07.049>.
 764 HIS Global Insight, 2014: The economic costs of disruption from a snowstorm. Study
 765 prepared for the American Highway Users Alliance, 9 pp,
 766 <https://www.highways.org/2014/02/economic-impact-of-snowstorms/>.
 767 Hock, T. F., and J. L. Franklin, 1999: The NCAR GPS Dropwindsonde, *Bull. Amer. Meteor.*
 768 *Soc.*, **80**(3), 407-420, [https://doi.org/10.1175/1520-](https://doi.org/10.1175/1520-0477(1999)080<0407:TNGD>2.0.CO;2)
 769 0477(1999)080<0407:TNGD>2.0.CO;2.
 770 Hou, A. Y., R. K. Kakar, S. Neeck, A. A. Azarbarzin, C. D. Kummerow, M. Kojima, R. Oki,
 771 K. Nakamura, and T. Iguchi, 2014: The Global Precipitation Measurement Mission. *Bull.*
 772 *Amer. Meteor. Soc.*, **95**, 701-722, <https://doi.org/10.1175/BAMS-D-13-00164.1>.

773 Houze, R. A., Jr., P. V. Hobbs, K. R. Biswas, and W. M. Davis, 1976: Mesoscale rainbands
 774 in Extratropical cyclones. *Mon. Wea. Rev.*, **105**, 868-878, [https://doi.org/10.1175/1520-0493\(1976\)104<0868:MRIEC>2.0.CO;2](https://doi.org/10.1175/1520-0493(1976)104<0868:MRIEC>2.0.CO;2).
 775
 776 Jensen, A. A., J. Y. Harrington, H. Morrison, and J. A. Milbrandt, 2017: Predicting Ice Shape
 777 Evolution in a Bulk Microphysics Model. *J. Atmos. Sci.*, **74**, 2081-2104,
 778 <https://doi.org/10.1175/JAS-D-16-0350.1>.
 779 Jurewicz, M. L., Sr., and M. S. Evans, 2004: A comparison of two banded, heavy snowstorms
 780 with very different synoptic settings. *Wea. Forecasting*, **19**, 1011-1028,
 781 <https://doi.org/10.1175/WAF-823.1>.
 782 Keeler, J. M., B. F. Jewett, R. M. Rauber, G. M. McFarquhar, R. M. Rasmussen, L. Xue, C.
 783 Liu, and G. Thompson, 2016a: Dynamics of cloud-top generating cells in winter
 784 cyclones. Part I: Idealized simulations in the context of field observations. *J. Atmos.*
 785 *Sci.*, **73**, 1507–1527, <https://doi.org/10.1175/JAS-D-15-0126.1>.
 786 Keeler, J. M., B. F. Jewett, R. M. Rauber, G. M. McFarquhar, R. M. Rasmussen, L. Xue, C.
 787 Liu, and G. Thompson, 2016b: Dynamics of cloud-top generating cells in winter
 788 cyclones. Part II: Radiative and instability forcing. *J. Atmos. Sci.*, **73**, 1529–1553,
 789 <https://doi.org/10.1175/JAS-D-15-0127.1>.
 790 Keeler, J. M., B. F. Jewett, R. M. Rauber, G. M. McFarquhar, R. M. Rasmussen, L. Xue, C.
 791 Liu, and G. Thompson, 2017: Dynamics of cloud-top generating cells in winter cyclones.
 792 Part III: Shear and convective organization. *J. Atmos. Sci.*, **74**, 2879-2897,
 793 <https://doi.org/10.1175/JAS-D-16-0314.1>.
 794 King, W. D., D. A. Parkin, and R. J. Handsworth, 1978: A hot-wired liquid water device
 795 having fully calculable response characteristics. *J. Appl. Meteor.*, **17**, 1809–1813,
 796 [https://doi.org/10.1175/1520-0450\(1978\)017<1809:AHWLWD>2.0.CO;2](https://doi.org/10.1175/1520-0450(1978)017<1809:AHWLWD>2.0.CO;2).

797 Kocin, P. J., and L. W. Uccellini, 2004: *Snowstorms along the northeastern coast of the*
798 *United States: 1955-1985*. Amer. Meteor. Soc. Meteorological Monographs, Boston,
799 Volume 22 (Num. 44), 280 pp.

800 Kollias, P., E. Luke, M. Oue, and K. Lamer, 2020: Agile adaptive radar sampling of fast-
801 evolving atmospheric phenomena guided by satellite imagery and surface cameras.
802 *Geophys. Res. Lett.*, **45**, e2020GL088440, <https://doi.org/10.1029/2020GL088440>.

803 Korolev, A. V., J. W. Strapp, G. A. Isaac, and A. N. Nevzorov, 1998: The Nevzorov airborne
804 hot-wire LWC–TWC probe: Principle of operation and performance characteristics. *J.*
805 *Atmos. Oceanic Technol.*, **15**, 1495–1510, [https://doi.org/10.1175/1520-](https://doi.org/10.1175/1520-0426(1998)015<1495:TNAHWL>2.0.CO;2)
806 0426(1998)015<1495:TNAHWL>2.0.CO;2.

807 Kroodsma, R. A., M. A. Fritts, J. F. Lucey, M. R. Schwaller, T. J. Ames, C. M. Cooke, and L.
808 M. Hilliard, 2019: CoSMIR Performance During the GPM OLYMPEX Campaign, *IEEE*
809 *Trans. Geosci. Remote Sens.*, **57**, 6397-6407,
810 <https://doi.org/10.1109/TGRS.2019.2906039>.

811 Kumar, B., P. Götzfried, N. Suresh, J. Schumacher, and R. A. Shaw, 2018: Scale dependence
812 of cloud microphysical response to turbulent entrainment and mixing. *J. Adv. Model.*
813 *Earth Syst.*, **10**, 2777– 2785, <https://doi.org/10.1029/2018MS001487>.

814 Kumjian, M. R., and K. A. Lombardo, 2017: Insights into the Evolving Microphysical and
815 Kinematic Structure of Northeastern U.S. Winter Storms from Dual-Polarization Doppler
816 Radar, *Mon. Wea. Rev.*, **145**, 1033-1061, <https://doi.org/10.1175/MWR-D-15-0451.1>.

817 Kumjian, M. R., S. A. Rutledge, R. M. Rasmussen, P. C. Kennedy, and M. Dixon, 2014:
818 High-resolution polarimetric radar observations of snow-generating cells. *J. Appl.*
819 *Meteor. Climatol.*, **53**, 1636-1658, <https://doi.org/10.1175/JAMC-D-13-0312.1>.

820 Lackmann, G. M., and G. Thompson, 2019: Hydrometeor Lofting and Mesoscale
821 Snowbands. *Mon. Wea. Rev.*, **147**, 3879-3899, [https://doi.org/10.1175/MWR-D-19-](https://doi.org/10.1175/MWR-D-19-0036.1)
822 0036.1.

823 Lamer, K., M. Oue, A. Battaglia, R. J. Roy, K. B. Cooper, R. Dhillon and P. Kollias, 2021:
824 First Light Multi-Frequency Observations with a G-band radar, *Atmos. Meas. Tech.*
825 *Discuss.* [preprint], <https://doi.org/10.5194/amt-2020-493>, in review.

826 Lance, S., C. A. Brock, D. Rogers, and J. A. Gordon, 2010: Water droplet calibration of the
827 cloud droplet probe (CDP) and in-flight performance in liquid, ice and mixed-phase
828 clouds during ARCPAC. *Atmos. Meas. Tech.*, **3**, 1683–1706, [https://doi.org/10.5194/amt-](https://doi.org/10.5194/amt-3-1683-2010)
829 3-1683-2010.

830 Lawson, R. P., R. E. Stewart, and L. J. Angus, 1998: Observations and numerical simulations
831 of the origin and development of very large snowflakes. *J. Atmos. Sci.*, **55**, 3209–3229,
832 [https://doi.org/10.1175/1520-0469\(1998\)055<3209:OANSOT>2.0.CO;2](https://doi.org/10.1175/1520-0469(1998)055<3209:OANSOT>2.0.CO;2).

833 Lawson, R. P., D. O'Connor, P. Zmarzly, K. Weaver, B. Baker, Q. Mo, and H. Jonsson,
834 2006: The 2D-S (Stereo) Probe: Design and Preliminary Tests of a New Airborne, High-
835 Speed, High-Resolution Particle Imaging Probe. *J. Atmos. Oceanic Technol.*, **23**, 1462-
836 1477, <https://doi.org/10.1175/JTECH1927.1>.

837 Li, L., G. Heymsfield, J. Carswell, D. Schaubert, M. McLinden, J. Creticos, M. Perrine, M.
838 Coon, J. Cervantes, M. Vega, S. Guimond, L. Tian, and A. Emory, 2015: The NASA
839 High-Altitude Imaging Wind and Rain Airborne Profiler (HIWRAP). *IEEE Trans.*
840 *Geosci. Remote Sens.*, **54**, 298-310, <https://doi.org/10.1109/TGRS.2015.2456501>.

841 Liao, L., R. Meneghini, A. Tokay, and L. F. Bliven, 2016: Retrieval of snow properties for
842 Ku- and Ka-Band Dual-Frequency Radar. *J. Appl. Meteor. Climatol.*, **55**, 1845-1858,
843 <https://doi.org/10.1175/JAMC-D-15-0355.1>.

844 Maahn, M., and P. Kollias, 2012: Improved Micro Rain Radar snow measurements using
845 Doppler spectra post-processing, *Atmos. Meas. Tech.*, **5**, 2661–2673,
846 <https://doi.org/10.5194/amt-5-2661-2012>.

847 Mace, G. G., and Q. Zhang, 2014: The CloudSat radar- lidar geometrical profile product
848 (RL- GeoProf): Updates, improvements, and selected results, *J. Geophys. Res. Atmos.*,
849 **119**, 9441– 9462, <https://doi.org/10.1002/2013JD021374>.

850 Mach, D. M., R. J. Blakeslee, M. G. Bateman, and J. C. Bailey, 2009: Electric fields,
851 conductivity, and estimated currents from aircraft overflights of electrified clouds, *J.*
852 *Geophys. Res.*, **114**, D10204, <https://doi.org/10.1029/2008JD011495>.

853 Matejka, T. J., R. A. Houze, Jr., and P. V. Hobbs, 1980: Microphysics and dynamics of
854 clouds associated with mesoscale rainbands in tropical cyclones. *Quart. J. Roy. Meteor.*
855 *Soc.*, **106**, 29-56, <https://doi.org/10.1002/qj.49710644704>.

856 Mason, S. L., R. J. Hogan, C. D. Westbrook, S. Kneifel, D. Moisseev, and L. von Terzi,
857 2019: The importance of particle size distribution and internal structure for triple-
858 frequency radar retrievals fo the morphology of snow. *Atmos. Meas. Tech.*, **12**, 4993-
859 5018, <https://doi.org/10.5194/amt-12-4993-2019>.

860 Matrosov, S. Y., a. J. Heymsfield, and Z. Wang, 2005: Dual-frequency radar ratio of
861 nonspherical atmospheric hydrometeors. *Geophys. Res. Lett.*, **32**, L13816,
862 <https://doi.org/10.1029/2005GL023210>.

863 McFarquhar, G. M., G. Zhang, M. R. Poellot, G. L. Kok, R. McCoy, T. Tooman, A. Fridlind,
864 and A. J. Heymsfield, 2007: Ice properties of single-layer stratocumulus during the
865 Mixed-Phase Arctic Cloud Experiment: 1. Observations. *J. Geophys. Res.*, **112**, D24201,
866 <https://doi.org/10.1029/2007JD008633>.

867 McGill, M. J., D. L. Hlavka, W. D. Hart, V. S. Scott, J. D. Spinhirne, and B. Schmid, 2002:
868 The Cloud Physics Lidar: Instrument description and initial measurement results.
869 *Appl. Opt.*, **41**, 3725–3734, <https://doi.org/10.1364/AO.41.003725>.

870 McGill, M. J., L. Li, W. D. Hart, G. M. Heymsfield, D. L. Hlavka, P. E. Racette, L. Tian, M.
871 A. Vaughan, and D. M. Winker, 2004: Combined lidar- radar remote sensing: Initial
872 results from CRYSTAL- FACE, *J. Geophys. Res.*, **109**, D07203,
873 <https://doi.org/10.1029/2003JD004030>.

874 McMurdie, L.A., G. Heymsfield, J. E. Yorks, and S. A. Braun, 2019: Investigation of
875 Microphysics and Precipitation for Atlantic Coast-Threatening Snowstorms (IMPACTS)
876 Collection [indicate subset used]. NASA EOSDIS Global Hydrology Resource Center
877 Distributed Active Archive Center, accessed 26 May 2021,
878 <http://dx.doi.org/10.5067/IMPACTS/DATA101>.

879 Midzak, N., J. E. Yorks, J. Zhang, B. van Diedenhoven, S. Woods, and M. McGill, 2020: A
880 classification of ice crystal habits using combined CPL and RSP observations during the
881 SEAC4RS campaign, *J. Atmos. Oceanic Technol.*, **37**, 2185-2196,
882 <https://doi.org/10.1175/JTECH-D-20-0037.1>.

883 Mitchell, D. L., 1988: Evolution of Snow-Size Spectra in Cyclonic Storms. Part I: Snow
884 Growth by Vapor Deposition and Aggregation, *J. Atmos. Sci.*, **45**, 3431-3451,
885 [https://doi.org/10.1175/1520-0469\(1988\)045<3431:EOSSSI>2.0.CO;2](https://doi.org/10.1175/1520-0469(1988)045<3431:EOSSSI>2.0.CO;2).

886 Mitrescu, C., J. M. Haynes, G. L. Stephens, S. D. Miller, G. M. Heymsfield, and M. J.
887 McGill 2005: Cirrus cloud optical, microphysical, and radiative properties observed
888 during the CRYSTAL-FACE experiment: A lidar-radar retrieval system, *J. Geophys.*
889 *Res.*, **110**, D09208, doi:10.1029/2004JD005605.

890 Morales, R. F., Jr., 2008: The historic Christmas 2004 south Texas snow event: Diagnosis of
 891 the heavy snow band. *Natl. Wea. Dig.*, **32**, 135–152,
 892 <http://nwafiles.nwas.org/digest/papers/2008/Vol32No2/Pg135-Morales.pdf>.
 893 National Academies of Sciences, Engineering, and Medicine (NASEM), 2018: *Thriving on*
 894 *Our Changing Planet: A Decadal Strategy for Earth Observation from Space*.
 895 Washington, DC: The National Academies Press, 716 pp.,
 896 <https://doi.org/10.17226/24938>.
 897 NOAA National Centers for Environmental Information (NCEI), 2020: State of the Climate:
 898 National Climate Report 2020 Winter Highlights. Accessed 27 May 2021,
 899 <https://www.ncdc.noaa.gov/sotc/national/202002#season-highlights>.
 900 Nicosia, D. J., and R. H. Grumm, 1999: Mesoscale band formation in three major
 901 northeastern United States snowstorms. *Wea. Forecasting*, **14**, 346–368,
 902 [https://doi.org/10.1175/1520-0434\(1999\)014<0346:MBFITM>2.0.CO;2](https://doi.org/10.1175/1520-0434(1999)014<0346:MBFITM>2.0.CO;2).
 903 Novak, D. R., L. F. Bosart, D. Keyser, and J. S. Waldstreicher, 2004: An observational study
 904 of cold season-banded precipitation in Northeast U.S. cyclones. *Wea. Forecasting*, **19**,
 905 993–1010, <https://doi.org/10.1175/815.1>.
 906 Novak, D. R., B. A. Colle, and S. E. Yuter, 2008: High-Resolution Observations and Model
 907 Simulations of the Life Cycle of an Intense Mesoscale Snowband over the Northeastern
 908 United States. *Mon. Wea. Rev.*, **136**, 1433–1456,
 909 <https://doi.org/10.1175/2007MWR2233.1>.
 910 Novak, D. R., B. A. Colle, and A. R. Aiyer, 2010: Evolution of mesoscale precipitation
 911 band environments within the comma head of northeast U.S. cyclones. *Mon. Wea. Rev.*,
 912 **138**, 2354–2374, <https://doi.org/10.1175/2010MWR3219.1>.
 913 Nystrom, R., S. J. Greybush, X. Chen, and F. Zhang, 2021: Potential for new constraints on
 914 tropical cyclone surface-exchange coefficients through simultaneous ensemble-based

915 state and parameter estimation. *Mon. Wea. Rev.*, **149**, 2213-2230.

916 <https://doi.org/10.1175/MWR-D-20-0259.1>.

917 Olson, W. S., L. Tian, M. Grecu, K.-S. Kuo, B. T. Johnson, A. J. Heymsfield, A. Bansemer,
 918 G. M. Heymsfield, J. R. Wang, and R. Meneghini, 2016: The Microwave Radiative
 919 Properties of Falling Snow Derived from Nonspherical Ice Particle Models. Part II: Initial
 920 Testing Using Radar, Radiometer and In Situ Observations, *J. Appl. Meteorol. Climatol.*,
 921 **55**(3), 709-722, <https://doi.org/10.1175/JAMC-D-15-0131.1>.

922 Oue, M., M. R. Kumjian, Y. Lu, J. Verlinde, K. Aydin, and E. E. Clothiaux, 2015: Linear
 923 Depolarization Ratios of Columnar Ice Crystals in a Deep Precipitating System over the
 924 Arctic Observed by Zenith-Pointing Ka-Band Doppler Radar, *J. Appl. Meteor. Climatol.*,
 925 **54**(5), 1060-1068, <https://doi.org/10.1175/JAMC-D-15-0012.1>.

926 Oue, M., P. Kollias, S. Y. Matrosov, A. Battaglia, A., and A. V. Ryzhkov, 2021:
 927 Combination Analysis of Multi-Wavelength, Multi-Parameter Radar Measurements for
 928 Snowfall, *Atmos. Meas. Tech. Discuss.*, <https://doi.org/10.5194/amt-2021-78>, in review.

929 Picca, J. C., D. M. Schultz, B. A. Colle, S. Ganetis, D. R. Novak, and M. J. Sienkiewicz,
 930 2014: The Value of Dual-Polarization Radar in Diagnosing the Complex Microphysical
 931 Evolution of an Intense Snowband. *Bull. Amer. Meteor. Soc.*, **95**, 1825–1834,
 932 <https://doi.org/10.1175/BAMS-D-13-00258.1>.

933 Pisano, P. A., L. C. Goodwin, and M. A. Rossetti, 2008: U.S. Highway crashes in adverse
 934 road weather conditions. *Proc. 88th Annual American Meteorological Society Meeting*,
 935 New Orleans, LA, Amer. Meteor. Soc.,
 936 https://ams.confex.com/ams/88Annual/techprogram/paper_133554.htm.

937 Plummer, D. M., G. M. McFarquhar, R. M. Rauber, B. F. Jewett, and D. Leon, 2014:
 938 Structure and statistical analysis of the microphysical properties of generating cells in the

939 comma-head region of continental winter cyclones. *J. Atmos. Sci.*, **71**, 4181-4203,
940 <https://doi.org/10.1175/JAS-D-14-0100.1>.

941 Plummer, D. M., G. M. McFarquhar, R. M. Rauber, B. F. Jewett, and D.
942 C. Leon, 2015: Microphysical properties of convectively generated fall streaks within the
943 stratiform comma head region of continental winter cyclones. *J. Atmos. Sci.*, **72**, 2465–
944 2483, <https://doi.org/10.1175/JAS-D-14-0354.1>.

945 Radford, J. T., G. M. Lackmann, and M. A. Baxter, 2019: An Evaluation of snowband
946 predictability in the High-Resolution Rapid Refresh. *Wea. Forecasting*, **34**, 1477-1494,
947 <https://doi.org/10.1175/WAF-D-19-0089.1>.

948 Rauber, R. M., and 11 co-authors, 2014: Stability and charging characteristics of the comma-
949 head region of continental winter cyclones. *J. Atmos. Sci.*, **71**, 1559-1582,
950 <https://doi.org/10.1175/JAS-D-13-0253.1>.

951 Rauber, R. M., S. M. Ellis, J. Vivekanandan, J. Stith, W-C Lee, G. M. McFarquhar, and B. F.
952 Jewett, 2017: Finescale structure of a snowstorm over the Northeastern United States: a
953 first look at high resolution HIAPER Cloud Radar Observations. *Bull. Amer. Meteor.*
954 *Soc.*, **98**, 253-269, <https://doi.org/10.1175/BAMS-D-15-00180.1>.

955 Rogers, R. R., and M. K. Yau, 1989: *A short course in cloud physics*. Oxford: Pergamon
956 Press, 304 pp.

957 Rosenow, A. A., D. M. Plummer, R. M. Rauber, G. M. McFarquhar, B. F. Jewett, and D.
958 Leon, 2014: Vertical Velocity and Physical Structure of Generating Cells and Convection
959 in the Comma Head Region of Continental Winter Cyclones. *J. Atmos. Sci.*, **71**, 1538–
960 1558. <https://doi.org/10.1175/JAS-D-13-0249.1>.

961 Rosenow, A.A., R.M. Rauber, G.M. McFarquhar and J.M. Keeler, 2018: Elevated potential
962 instability in the comma-head: Distribution and development. *Mon. Wea. Rev.*, **146**, 1259-
963 1278. <https://doi.org/10.1175/MWR-D-17-0283.1>.

964 Ryzhkov, A., P. Zhang, H. Reeves, M. Kumjian, T. Tschallener, S. Trömel, and C. Simmer,
 965 2016: Quasi-Vertical Profiles—A New Way to Look at Polarimetric Radar Data. *J. Atmos.*
 966 *Oceanic Technol.*, **33**, 551-562, <https://doi.org/10.1175/JTECH-D-15-0020.1>.
 967 Sanders, F., and L. F. Bosart, 1985: Mesoscale structure in the megalopolitan snowstorm, 11-
 968 12 February 1983. Part II: Doppler radar study of the New England snowband. *J. Atmos.*
 969 *Sci.*, **42**, 1398-1407, [https://doi.org/10.1175/1520-](https://doi.org/10.1175/1520-0469(1985)042<1398:MSITMS>2.0.CO;2)
 970 [0469\(1985\)042<1398:MSITMS>2.0.CO;2](https://doi.org/10.1175/1520-0469(1985)042<1398:MSITMS>2.0.CO;2).
 971 Schultz, C. J., S. S. Harkema, D. M. Mach, M. Bateman, T. J. Lang, G. M. Heymsfield, M. L.
 972 McLinden, L. Li, M. Poellot, and K. Sand, 2021: Remote sensing of electric fields
 973 observed within winter precipitation during the 2020 Investigation of Microphysics and
 974 Precipitation for Atlantic Coast-Threatening Snowstorms (IMPACTS) field campaign. *J.*
 975 *Geophys. Res. Atmos.*, 126, e2021JD034704, <https://doi.org/10.1029/2021JD034704>.
 976 Schultz, D. M., and P. N. Schumacher, 1999: The Use and Misuse of Conditional Symmetric
 977 Instability, *Mon. Wea. Rev.*, **127**, 2709-2732, [https://doi.org/10.1175/1520-](https://doi.org/10.1175/1520-0493(1999)127<2709:TUAMOC>2.0.CO;2)
 978 [0493\(1999\)127<2709:TUAMOC>2.0.CO;2](https://doi.org/10.1175/1520-0493(1999)127<2709:TUAMOC>2.0.CO;2).
 979 Schultz, D. M., and J. A. Knox, 2007: Banded Convection Caused by Frontogenesis in a
 980 Conditionally, Symmetrically, and Inertially Unstable Environment, *Mon. Wea. Rev.*,
 981 135(6), 2095-2110, <https://doi.org/10.1175/MWR3400.1>.
 982 Skofronick-Jackson, and 17 co-authors, 2017: The Global Precipitation Measurement (GPM)
 983 mission for science and society. *Bull. Amer. Meteor. Soc.*, **98**, 1679-1695,
 984 <https://doi.org/10.1175/BAMS-D-15-00306.1>.
 985 Spencer, R. W., R. E. Hood, F. J. LaFontaine, E. A. Smith, R. Platt, J. Galliano, V. L. Griffin,
 986 E. Lobl, 1994: High-Resolution imaging of rain systems with the Advanced Microwave
 987 Precipitation Radiometer. *J. Atmos. Oceanic Technol.*, **11**, 49–857,
 988 [https://doi.org/10.1175/1520-0426\(1994\)011<0849:HRIORS>2.0.CO](https://doi.org/10.1175/1520-0426(1994)011<0849:HRIORS>2.0.CO).

989 Trapp, J. R., D. M. Schultz, A. V. Ryzhkov, and R. L. Holle, 2001: Multiscale structure and
 990 evolution of an Oklahoma winter precipitation event. *Mon. Wea. Rev.*, **129**, 486–501,
 991 [https://doi.org/10.1175/1520-0493\(2001\)129<0486:MSAEOA>2.0.CO;2](https://doi.org/10.1175/1520-0493(2001)129<0486:MSAEOA>2.0.CO;2).
 992 Waitz, F., M. Schnaiter, T. Leisner, and E. Jarvinen 2020: PHIPS-HALO: the airborne
 993 particle habit imaging and polar scattering probe - Part 3: Single Particle Phase
 994 Discrimination and Particle Size Distribution based on Angular Scattering Function.
 995 *Atmos. Meas. Tech.*, <https://doi.org/10.5194/amt-2020-297>.
 996 Walker-McLinden, M. L., L. Li, G. M. Heymsfield, M. Coon, and A. Emory 2021: The
 997 NASA/GSFC 94 GHz Airborne Solid State Cloud Radar System (CRS). *J. Atmos.*
 998 *Oceanic Technol.*, **38**, 1001-1017, <https://doi.org/10.1175/JTECH-D-20-0127.1>.
 999 Weinman, J. A., & Guetter, P. J. (1977). Determination of rainfall distributions from
 1000 microwave radiation measured by the Nimbus 6 ESMR. *Journal of Applied Meteorology*
 1001 and *Climatology*, 16(4), 437-442, [https://doi.org/10.1175/1520-](https://doi.org/10.1175/1520-0450(1977)016<0437:DORDFM>2.0.CO;2)
 1002 [0450\(1977\)016<0437:DORDFM>2.0.CO;2](https://doi.org/10.1175/1520-0450(1977)016<0437:DORDFM>2.0.CO;2).
 1003 Wolfsberg, D. G., K. A. Emanuel, and R. E. Passarelli, 1986: Band formation in a New
 1004 England Winter storm. *Mon. Wea. Rev.*, **114**, 1552-1569, [https://doi.org/10.1175/1520-](https://doi.org/10.1175/1520-0493(1986)114<1552:BFIANE>2.0.CO;2)
 1005 [0493\(1986\)114<1552:BFIANE>2.0.CO;2](https://doi.org/10.1175/1520-0493(1986)114<1552:BFIANE>2.0.CO;2).
 1006 Yorks, J. E., D. L. Hlavka, W. D. Hart, and M. J. McGill, 2011: Statistics of cloud optical
 1007 properties from airborne lidar measurements. *J. Atmos. Oceanic Technol.*, **28**, 869–883,
 1008 <https://doi.org/10.1175/2011JTECHA1507.1>.
 1009 Yuter, S. E. and R. A. Houze, Jr., 1995: Three-dimensional kinematic and microphysical
 1010 evolution of Florida cumulonimbus. Part II: Frequency distributions of vertical velocity,
 1011 reflectivity, and differential reflectivity. *Mon. Wea. Rev.*, **123**, 1641-1963.
 1012 [https://doi.org/10.1175/1520-0493\(1995\)123<1641:TDKAME>2.0.CO;2](https://doi.org/10.1175/1520-0493(1995)123<1641:TDKAME>2.0.CO;2)

1013 Zhang, F., C. A. Davis, M. L. Kaplan, S. E. Koch, 2001: Wavelet analysis and the governing
1014 dynamics of a large-amplitude mesoscale gravity-wave event along the East Coast of the
1015 United States. *Quart. J. Roy. Met. Soc.*, **127**, 2209-2245.
1016 <https://doi.org/10.1002/qj.49712757702>.

1017 Zhang, F., S. E. Koch, M. L. Kalpan, 2003: Numerical simulations of a large-amplitude
1018 mesoscale gravity wave event. *Meteorol. Atmos. Phys.*, **84**, 199-216.
1019 <https://doi.org/10.1007/s00703-002-0594-2>.

1020 Zhang, F., C. Snyder, and R. Rotunno, 2002: Mesoscale predictability of the “surprise”
1021 snowstorm of 24-25 January 2000. *Mon. Wea. Rev.*, **130**, 1617-1632,
1022 [https://doi.org/10.1175/1520-0493\(2002\)130<1617:MPOTSS>2.0.CO;2](https://doi.org/10.1175/1520-0493(2002)130<1617:MPOTSS>2.0.CO;2).

1023 Zhang, Y., D. J. Stensrud, and F. Zhang, 2019: Simultaneous Assimilation of Radar and All-
1024 Sky Satellite Infrared Radiance Observations for Convection-Allowing Ensemble
1025 Analysis and Prediction of Severe Thunderstorms. *Mon. Wea. Rev.*, **147**, 4389-4409.
1026 <https://doi.org/10.1175/MWR-D-19-0163.1>.

1027 Zhang, F., Y. Weng, J. A. Sippel, Z. Meng, and C. H. Bishop, 2009: Cloud-resolving
1028 Hurricane Initialization and Prediction through Assimilation of Doppler Radar
1029 Observations with an Ensemble Kalman Filter. *Mon. Wea. Rev.*, **137**, 2105-2125.
1030 <https://doi.org/10.1175/2009MWR2645.1>

1031

1032

1033 Table 1: Instruments flown on the ER-2 during the 2020 IMPACTS deployment. *See
1034 McMurdie et al. (2019) for instrument dataset.

Instrument PI/Organization	Instrument Characteristics	Derived Data Products	Reference
Advanced Microwave Precipitation	Cross-track scanning microwave radiometer at 10, 19, 37, 85 GHz	Precipitation characteristics, path integrated LWC and IWC	Spencer et al. (1994), Amiot et al. (2021)

Radiometer (AMPR) - T. Lang/MSFC			
Cloud Physics Lidar (CPL) - M. McGill/GSFC	Attenuated backscatter at 355, 532, 1064 nm; volume depolarization ratio at 1064 nm	Cloud/aerosol layer boundaries, cloud/aerosol optical depth, extinction, and depolarization; detection of cloud phase at cloud top	McGill et al. (2002)
Cloud Radar System (CRS) - M. McLinden/GSFC	<u>W-band</u> nadir-pointing Doppler radar with minimum detectable threshold of –30 dBZ @ 10 km altitude; Linear Depolarization	Vertical velocity, precipitation rates, phase, hydrometeor size, various vertical profile characteristics	Walker-McLinden et al. (2021)
Conical Scanning Millimeter-wave Imaging Radiometer (CoSMIR) - R. Kroodsma/GSFC	Conical and/or Cross-track scanning passive microwave radiometer at ~50, 89, 165.5, & 183 GHz	Precipitation characteristics, path integrated LWC and IWC	Kroodsma et al. (2019)
ER-2 X-Band Doppler Radar (EXRAD) - G. Heymsfield/GSFC	<u>X-band</u> nadir & conical scanning Doppler radar with minimum detectable threshold of –12 dBZ /-3 dBZ (nadir/scanning) @ 10 km range	Vertical velocity, precipitation rates, phase, hydrometeor size, various vertical profile characteristics, horizontal winds	*
High-altitude Imaging Wind and Rain Airborne Profiler (HIWRAP) - L. Li/GSFC	<u>Ku- and Ka-band</u> nadir-pointing Doppler radars with minimum detectable threshold of –10 dBZ (Ku) and –12 dBZ (Ka) @ 10 km altitude; Linear Depolarization	Vertical velocity, precipitation rates, phase, hydrometeor size, various vertical profile characteristics	Li et al. (2015)
Lightning Instrument Package (LIP) - C. Schultz/MSFC	Electric Field	Vector electric field and changes due to lightning occurrence	Mach et al. (2009)

1036 Table 2: Instruments flown on the P-3 during the 2020 IMPACTS deployment. *See
 1037 McMurdie et al. (2019) for instrument dataset.

Instrument - PI/Organization	Instrument Characteristics	Derived Data Products	Reference
Turbulent Air Motion Measurement System (TAMMS) - K. Thornhill/LaRC	In-situ measurement systems designed to acquire high-frequency state parameters	Flight level 3D-wind vector, temperature, humidity	Barrick et al. (1996)
Advanced Vertical Atmospheric Profiling System (AVAPS) - K. Thornhill/LaRC	Expendable GPS-tracked device dropped from aircraft to measure in-situ profiles	Vertical profiles of pressure, temperature, relative humidity, and winds	Hock et al. (1999)
Cloud-Droplet Probe (CDP) - M. Poellot/UND	Particle samples in 2-50 μm size range	Concentration and size distribution of cloud droplets	Lance et al. (2010)
Particle Habit Imaging and Polar Scattering (PHIPS) - M. Schnaiter/KIT	High resolution particle information up to ~ 700 μm size range	2D particle images, Single particle phase discrimination and particle size distribution up to ~ 700 μm size range	Abdelmonem et al. (2016) Waitz et al. (2020)
2D-Stereo Probe (2DS) - M. Poellot/UND	Particle samples in 10 μm to 3 mm size range	Droplet, Ice Particle Size Distributions, 3D particle images	Lawson et al. (2006)
High-Volume Precipitation Spectrometer-3 (HVPS-3) - M. Poellot/UND	Particle samples in 150 μm to 10 cm size range	Droplet, Ice Particle Size Distributions, 2D projections of 3D particle images	Lawson et al. (1998)
Nevzorov Probe - M. Poellot/UND	Cloud liquid and total condensate up to 2 g m^{-3}	Liquid & Ice Water Content	Korolev et al. (1998)
King Probe - M. Poellot/UND	Liquid water probe, up to 2 g m^{-3} , for cloud droplet sizes of 2-30 μm	Liquid Water Content	King et al. (1978)
Hawkeye Probe - M. Poellot/UND	Multi-probe sensor (FastCDP, 2DS, CPI)	Droplet, Ice Particle Size Distributions, 3D particle images	*
Rosemont Icing Detector (RICE) - M. Poellot/UND	Supercooled liquid water measurements in excess of 0.01 g m^{-3}	Presence and approximate amount of supercooled liquid water	Claffey et al. (1995)
Water Isotope System for Precipitation and Entrainment Research (WISPER) - D. Toohey/U. Colo	Total Ice measurements up to 2 g m^{-3}	Cloud particle concentration, condensate mass, water vapor, ice water content	Herman et al. (2020)

1038

1039 Table 3: Ground observations and instruments used during the 2020 IMPACTS deployment.

1040 *See McMurdie et al. (2019) for instrument dataset.

1041

Instrument - PI/Organization	Location	Geophysical Quantities Measured	Measurement Details	Reference
Mobile rawinsondes - Lead by UIUC and SBU	Various locations in NY, New England, Illinois	P, T, wind direction, wind speed, Td		*
Fixed NOAA rawinsondes J. Walstreicher (lead)/NWS	Fixed NWS sounding locations	P, T, wind direction, wind speed, Td		*
Parsivel P. Kollias/SBU	SBU/Mobile truck	Particle size distribution, particle fall speed	Optical disdrometer	Friedrich et al. (2013)
Pluvio2 P. Kollias/SBU	SBU	Precipitation amount	Weighing gauge 1 min frequency	*
MRRR P. Kollias/SBU	SBU/Mobile truck	Precipitation intensity, fall speed and vertical air motion	K-band profiling radar (4 s, 60 m resolutions)	Maahn and Kollias (2012), Oue et al. (2021)
Ceilometers P. Kollias/SBU	SBU/Mobile truck	cloud location	Profiling lidar backscatter 15 s, 10- 60 m resolution	*
KASPR P. Kollias/SBU	SBU	Precipitation intensity, particle fall speed, wind, and vertical air motion, precipitation particle shape	VPT, PPI, and RHI measurements by Ka-band scanning polarimetric radar at high temporal and spatial resolutions	Kollias et al. (2020)
ROGER P. Kollias/SBU	SBU	Precipitation intensity, particle fall speed and vertical air motion	W-band profiling radar, 4 s and 30 m resolutions	Lamer et al. (2021)
MWR P. Kollias/SBU	SBU	liquid water path	microwave radiometer	*
SKYLER P. Kollias/SBU	SBU/Mobile truck	Precipitation intensity, precipitation particle fall speed and vertical air motion, precipitation particle shape	X-band phased array radar	Kollias et al. (2020)

WFF D3R, PIP, MRR, Pluvio, Parsivel, Wolff/WFF	Wallops, VA	Reflectivity, Doppler velocity, and polarimetric information	Scanning Ku- and Ka-band radar	Kumar et al. (2018)
NYS Mesonet J. Brotzge/ SUNY Albany	NY State various locations	Surface meteorology and SWE, profiles of T, V, rh, liquid water	Surface observations 1 min frequency. Profiling stations	Brotzke et al. (2020)

Table 4: Description of the storms sampled during the 2020 IMPACTS deployment.

Date	Aircraft	Event Description
18 January	P-3	Snowbands in prefrontal sector of mature cyclone over upstate NY
25 January	P-3, ER-2	Warm occluded front with generating cells
01 February	P-3, ER-2	Warm oceanic frontal system over southern Atlantic with GPM overpass
05 February	P-3, ER-2	Shallow frontal zone over Midwest with snowbands
07 February	P-3, ER-2	Heavy snow and multiple bands in a rapidly deepening cyclone over New England and New York
13 February	P-3	Warm front overrunning precipitation with multiple wave structures
18 February	P-3	Moisture overrunning a warm front with snow over Vermont and Maine
20 February	P-3	Coastal cyclogenesis with snowbands across North Carolina
25 February	P-3, ER-2	Generating cells with supercooled water in a NW sector of a Midwest Storm
27 February	ER-2	Snowbands wrap around a deep occluded cyclone over northern NY

Figures

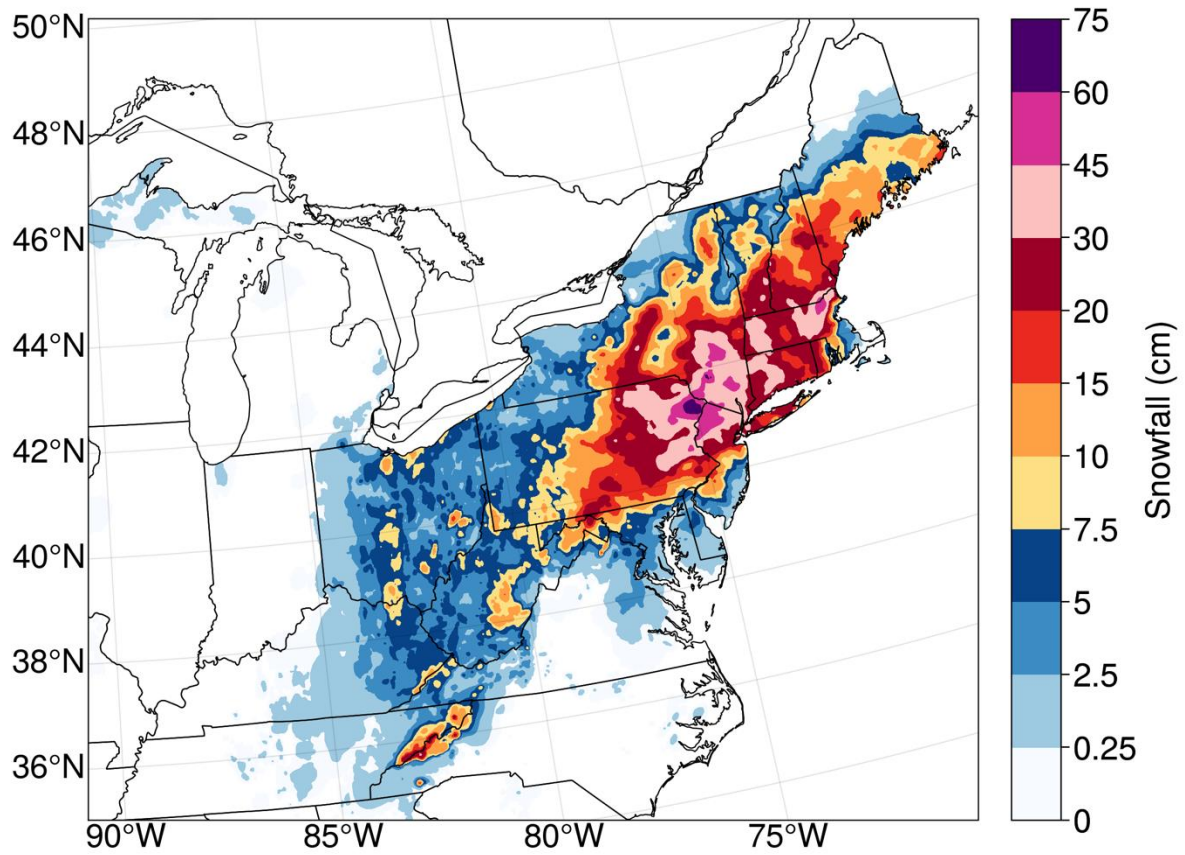


Figure 1: Snowfall totals in cm for the period 1200 UTC 1 February – 1200 UTC 2 February 2021. Data source: National Operational Hydrologic Remote Sensing Center snowfall analysis version 2 obtained from https://www.nohrsc.noaa.gov/snowfall_v2/.

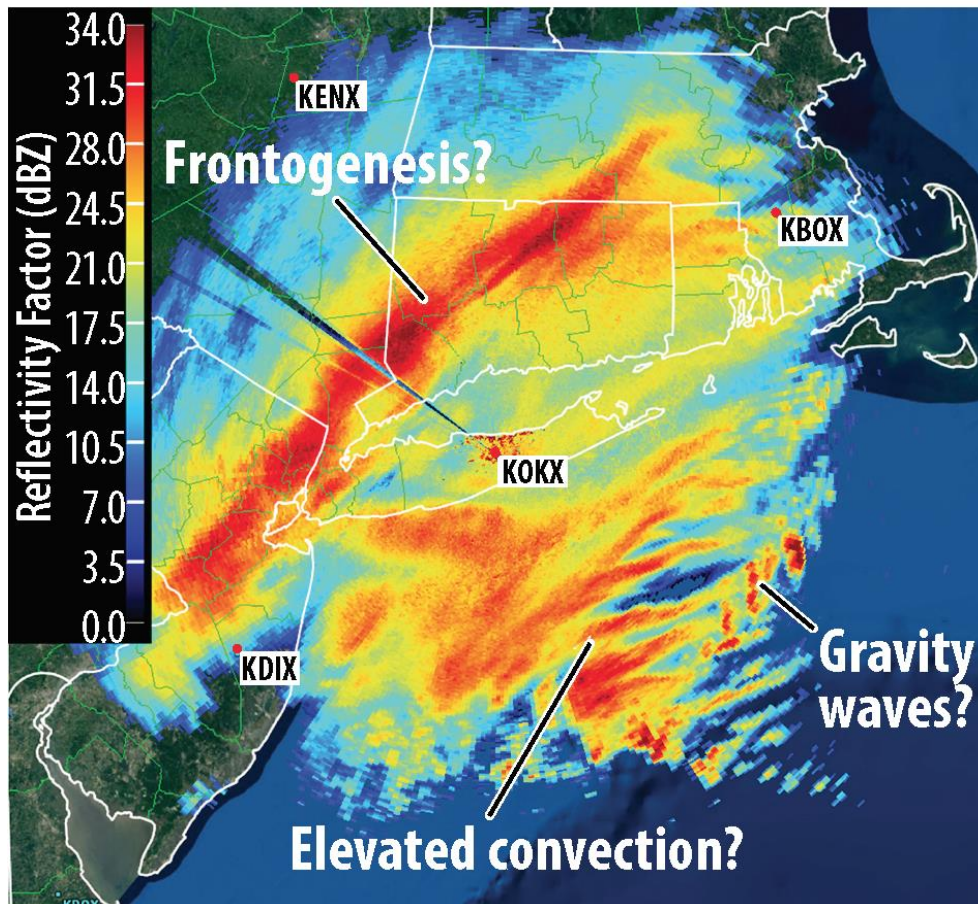


Figure 2: An example plot of radar reflectivity factor (dBZ) illustrating narrow regions of high reflectivity associated with the primary snowband and multi-bands. Potential mechanisms contributing to snowband formation and maintenance are indicated on the figure.

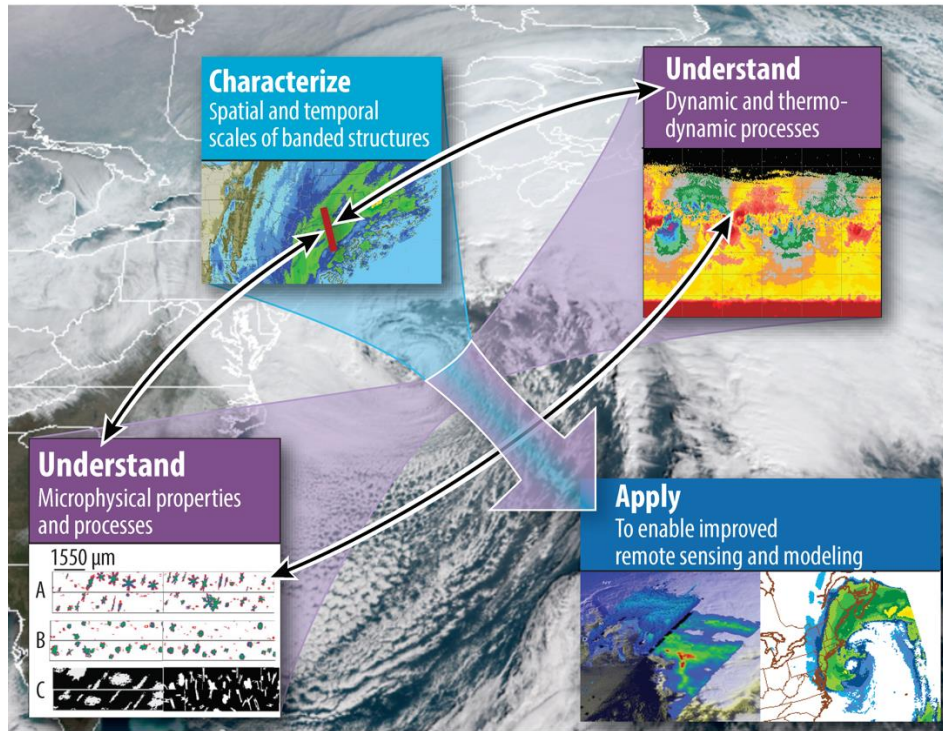


Figure 3: IMPACTS goals illustrated through graphics overlaying an intense winter cyclone over the North Atlantic.

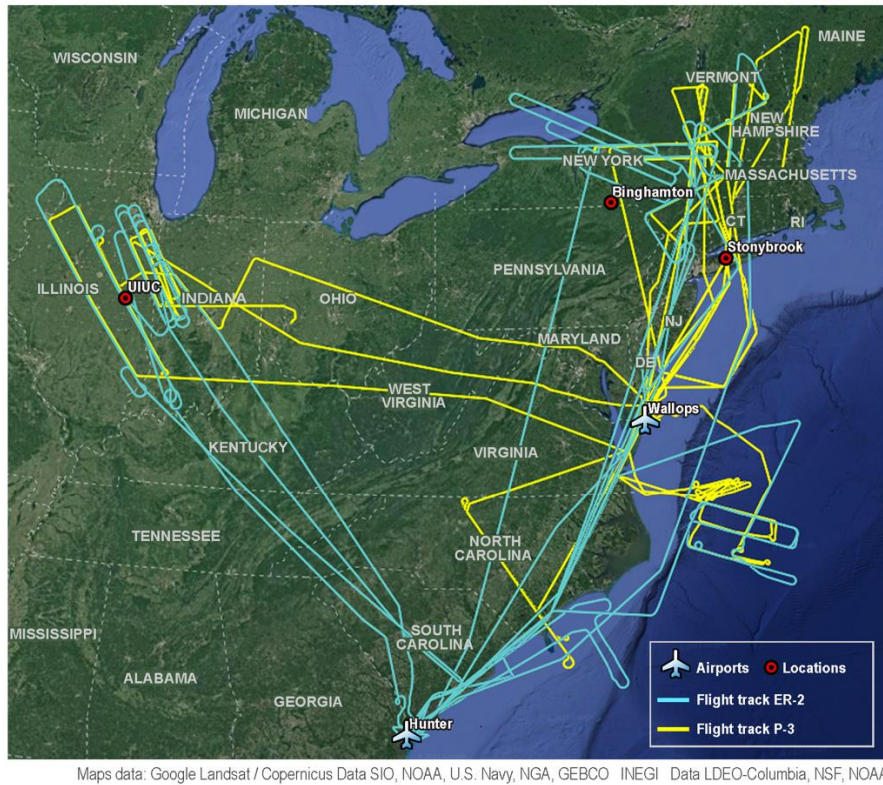


Figure 4: Flight tracks of the ER-2 (blue) and P-3 (yellow) during the 2020 IMPACTS deployment. Airplane symbols indicate airfields used in 2020, Wallops (P-3) and Hunter (ER-2). Red dots indicate home-base locations used for mobile sounding launches.

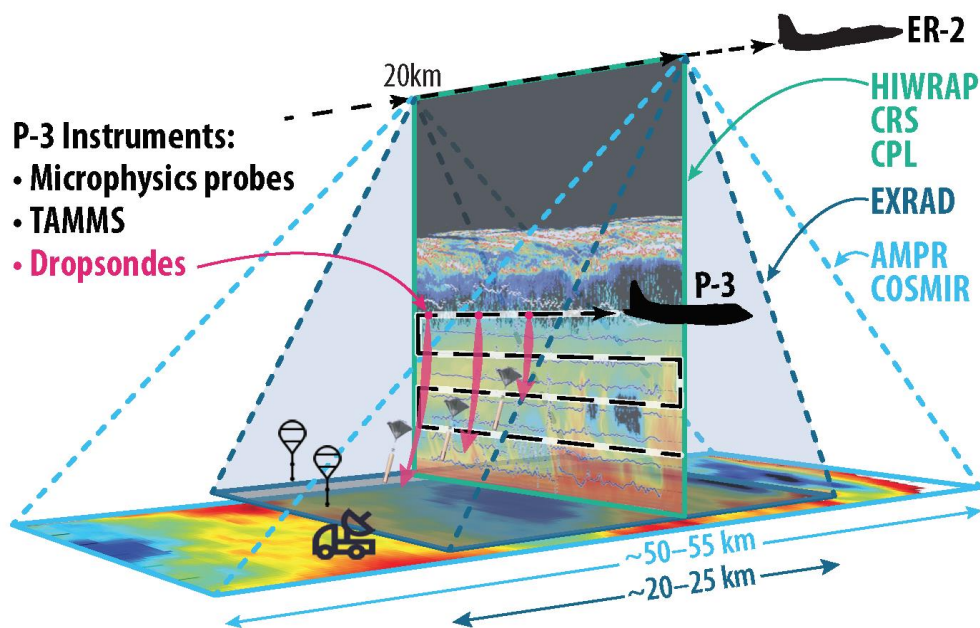


Figure 5: Illustration of the observational strategy for IMPACTS. The satellite-simulating ER-2 flies above the storm and samples with passive and active remote sensing instruments (sampling width of the different instruments indicated with dashed colored lines; see Table 1 for list of instruments) while the P-3 flies within the storm at different altitudes, releasing dropsondes over water. Surface radars and mobile soundings are represented by the balloons and truck symbols.

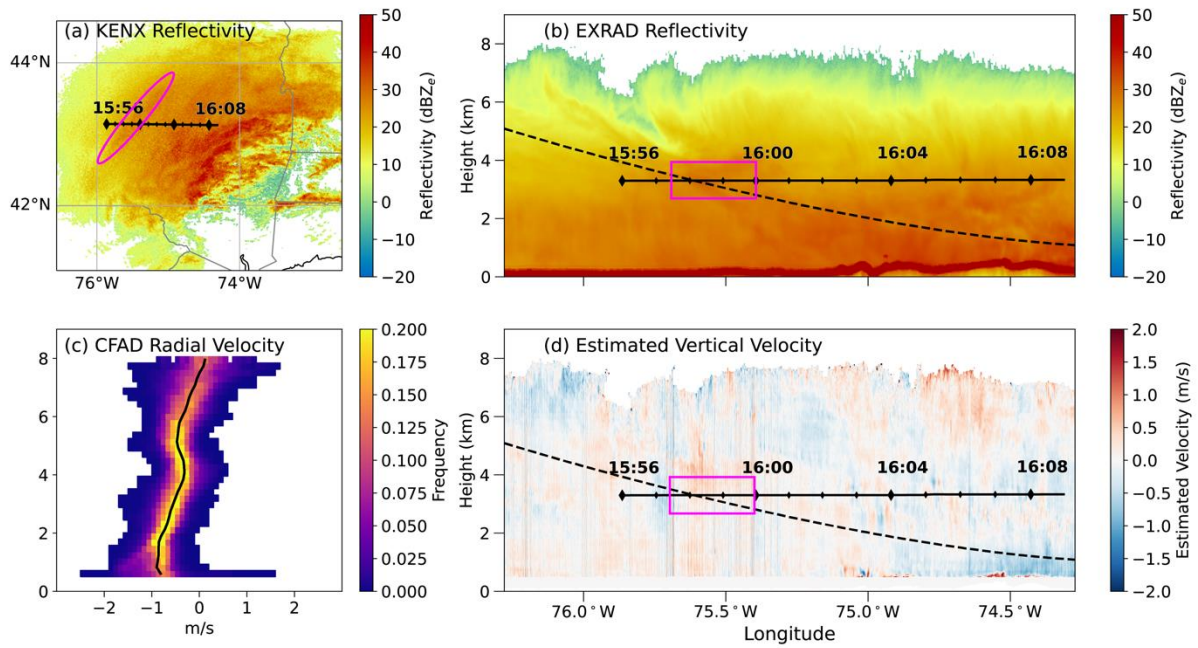


Figure 6: Comparison of radar reflectivity (dBZ) from the NWS WSR-88D radar and the ER-2 radars for the 7 February 2020 event: (a) Albany (KENX) reflectivity from a PPI scan at 0.9° taken at 1603 UTC; (b) EXRAD reflectivity (dBZ) ; (c) Contoured Frequency by Altitude Diagram of the radial velocity measured by the HIWRAP Ka-band radar with the median drawn as a black line, and (d) estimated vertical velocity (m s^{-1}) calculated by adding the median radial velocity at each altitude as shown in (c) to the nadir pointing beam of the HIWRAP Ka-band radial velocity. The location and times of the P-3 flight leg are shown by the horizontal black line in panels (a), (b) and (d) and the height of the KENX scan is indicated by the dashed curved line in (b) and (d). Feature of interest discussed in text is indicated with magenta boxes or ellipse. The dark red thick line at the bottom of the figure in (b) is the ground.

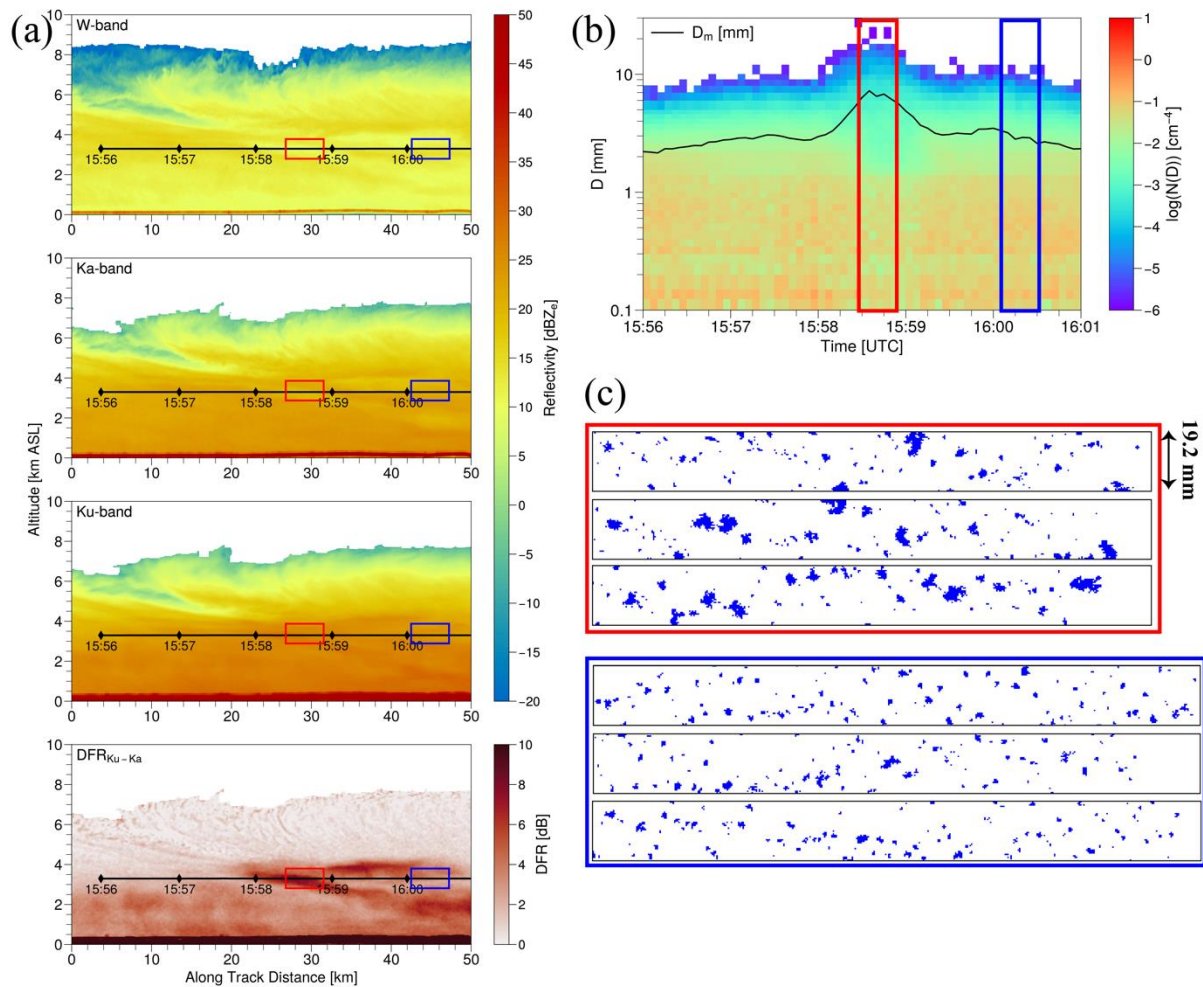


Figure 7: Comparison of cross-sections of radar reflectivity from the ER-2 radars and microphysical measurements from the P-3. (a) Radar reflectivity from the W-, Ku- and Ka-band wavelengths of the ER-2 radars and the Dual Frequency Ratio between the Ku- and Ka-bands in the bottom panel. (b) Particle size distribution (shaded) and mass-weighted mean diameter, D_m (black line). (c) 10-second particle imagery strips from the HVPS on the P-3. The red boxes indicate a time of relative enhanced reflectivity for all radars and enhanced DFR, and the blue boxes indicate a time outside of this enhancement.

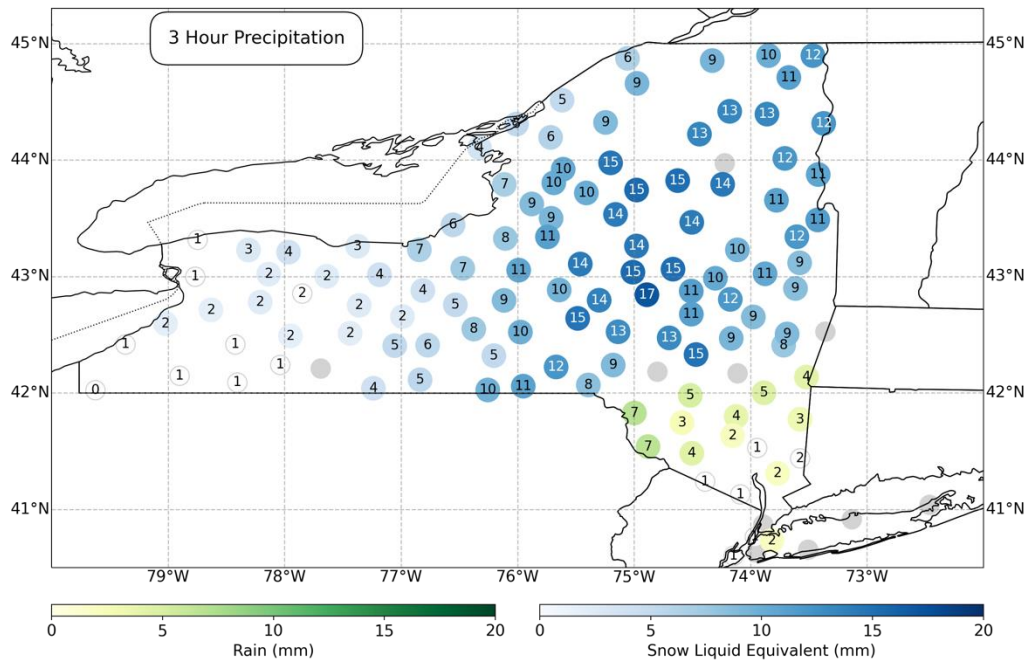


Figure 8: Three-hour precipitation totals (mm) from 1500 – 1800 UTC 7 February 2020 as measured at NYS mesonet stations. Blue circles indicate stations where precipitation fell as snow and green circles where precipitation fell as rain.

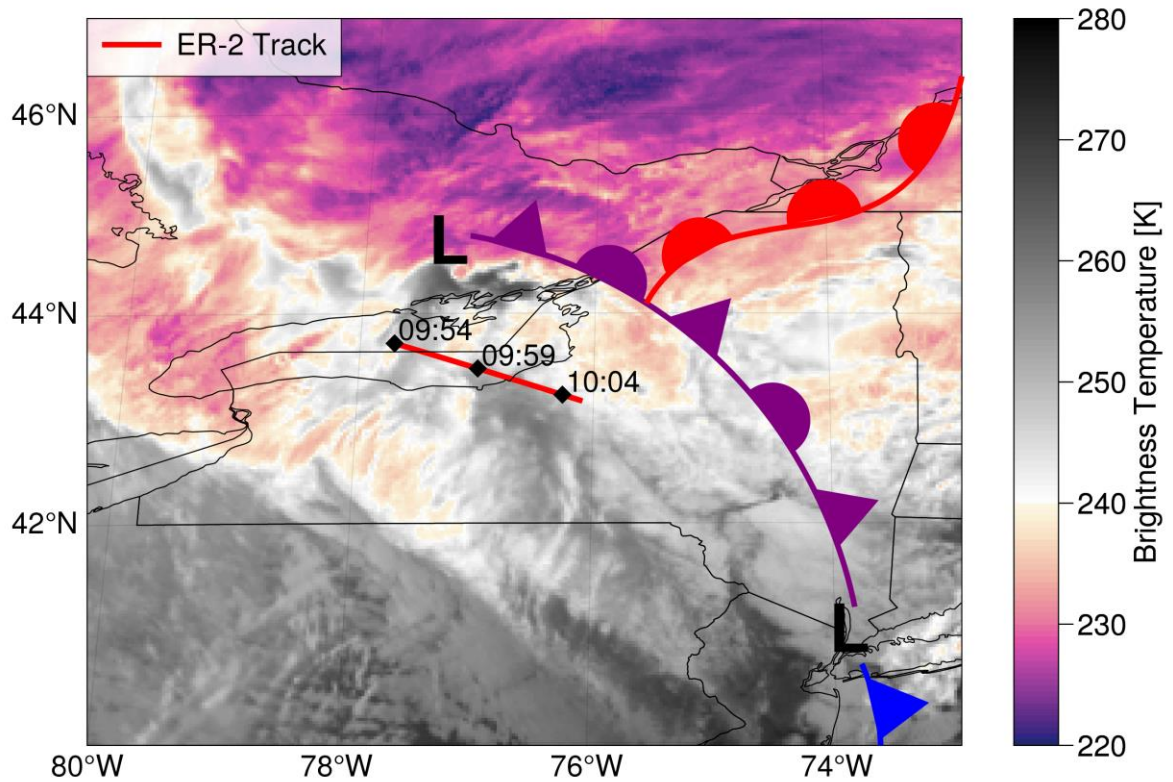


Figure 9: Infrared brightness temperatures from the Advanced Baseline Imager channel 13 of GOES-16 (color shades) at 1000 UTC 27 February 2020 with the ER-2 flight track as a red line with times overlaid. The overlaid frontal analysis with standard frontal symbols is valid 1000 UTC and is based on interpolating the 0900 and 1200 UTC 27 February 2020 National Weather Service Weather Prediction Center surface analyses.

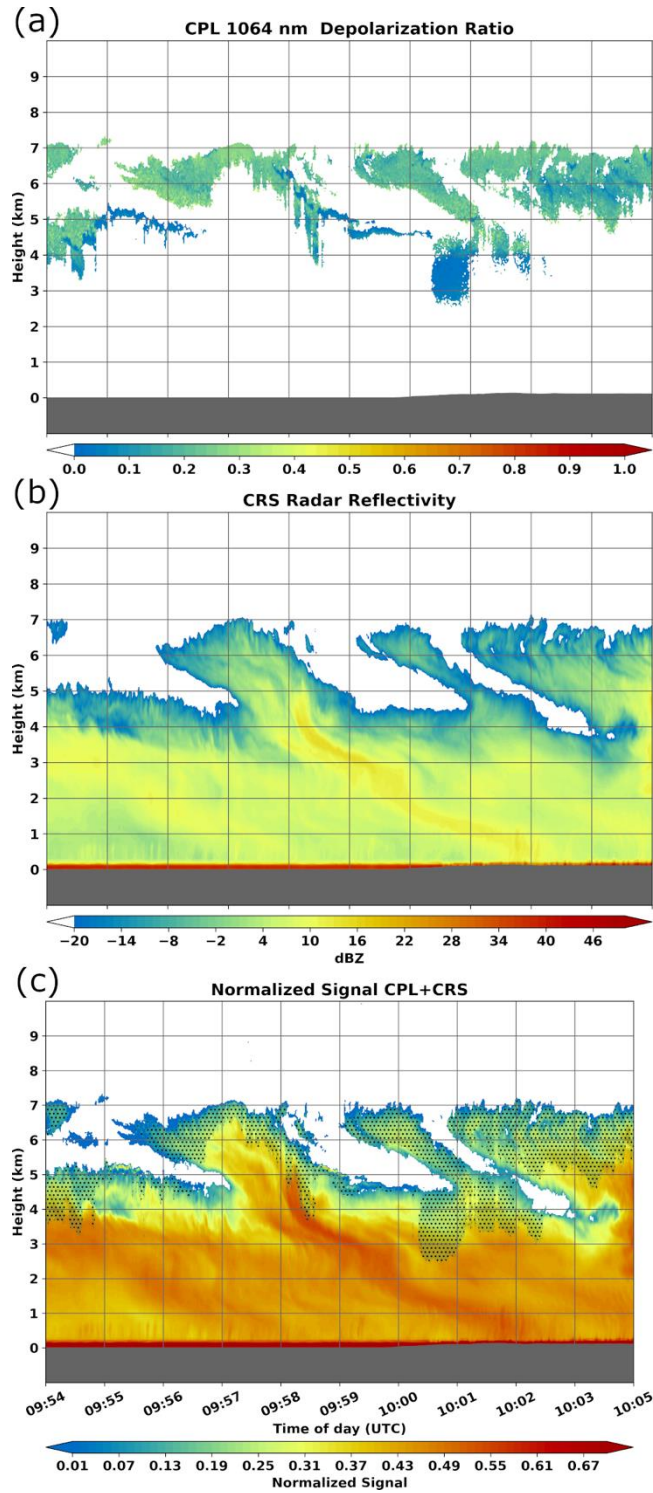


Figure 10: CPL and CRS and combined CPL-CRS signal from the 0954 – 1005 UTC 27 February 2020 ER-2 flight leg. (a) Attenuated total backscatter from the CPL, (b) CRS reflectivity, and (c) normalized signal from the CPL and CRS where stippling indicates overlap between the two instruments.

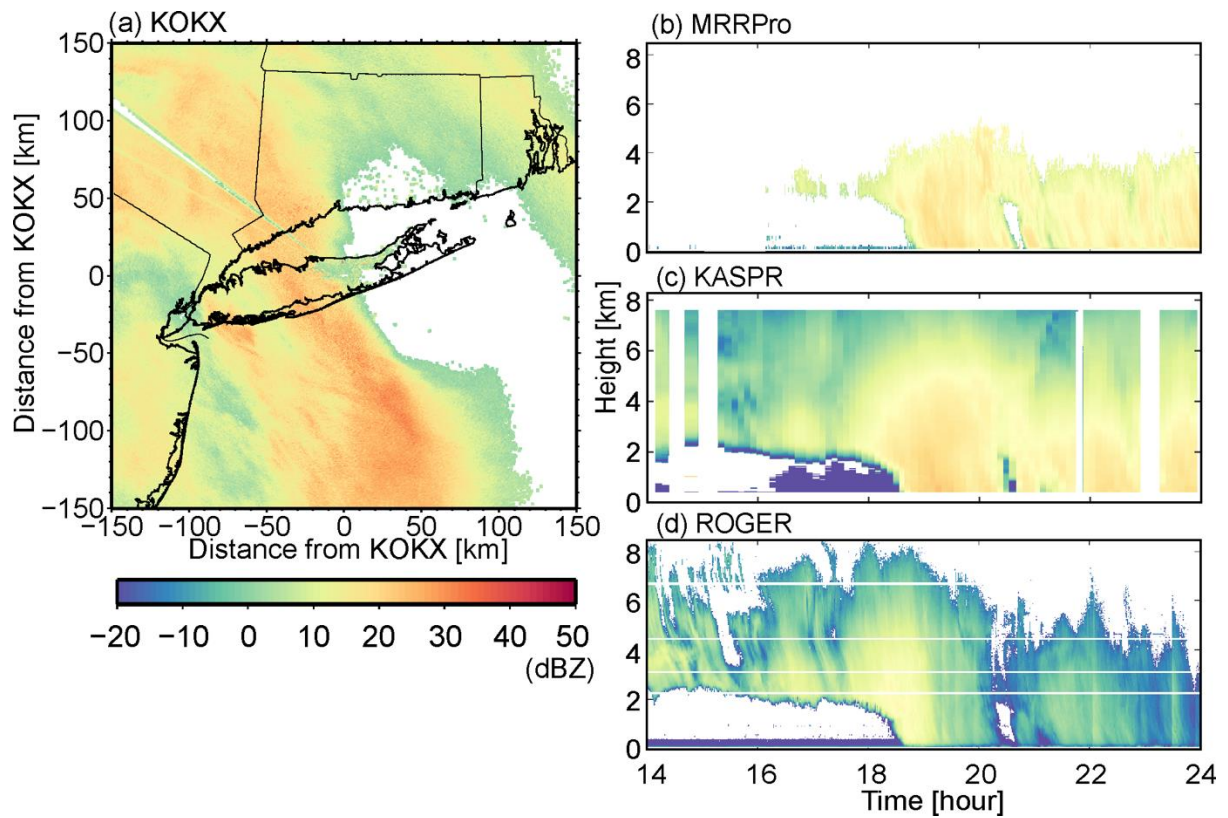


Figure 11: Radar sampling of the 18 January 2020 event from the Stony Brook radar site. (a) Radar reflectivity from the KOKX WSR-88D radar on Long Island at the 0.5° elevation angle at 1904 UTC, and height-time cross-sections of (b) MRRPro reflectivity at Cedar Beach (c) quasi-vertical pointing KASPR reflectivity at SBU and (d) ROGER (W-band) reflectivity from 1400 – 2359 UTC.

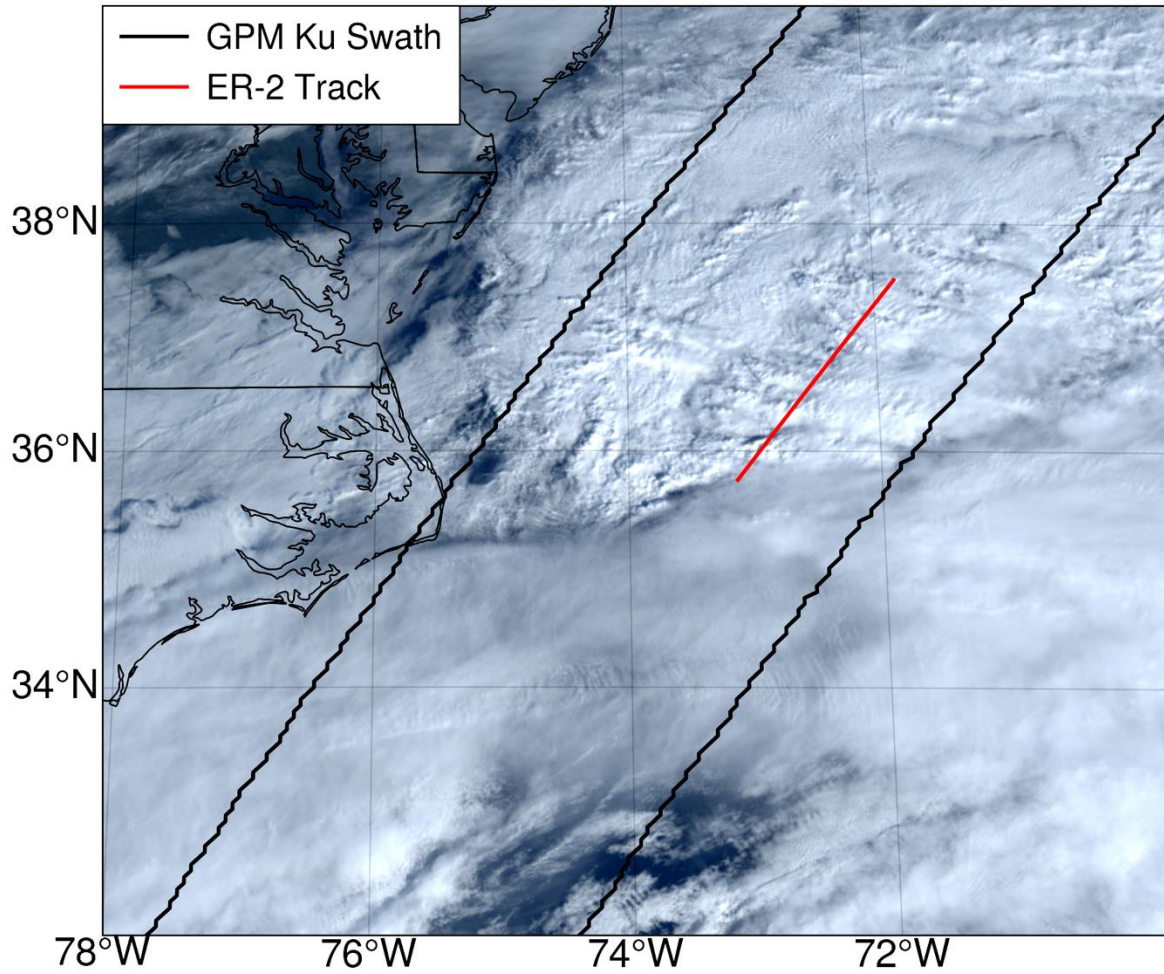
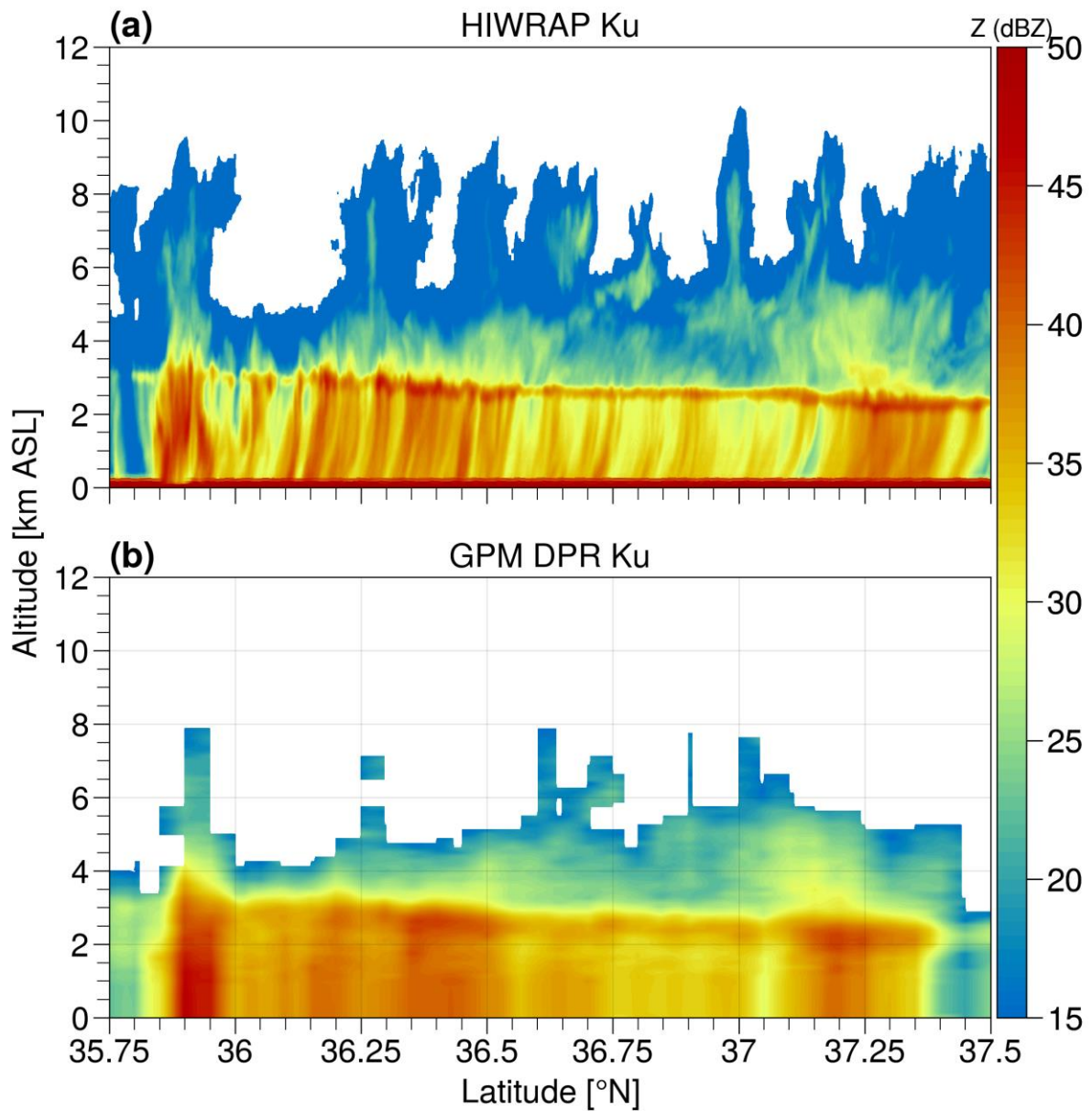


Figure 12: Visible imagery from the GOES-16 satellite for 1440 UTC 1 February 2020 during the time of the GPM overpass. The GPM Ku-band swath is shown with black lines and the coincident track of the ER-2 aircraft is shown with a red line.

1141



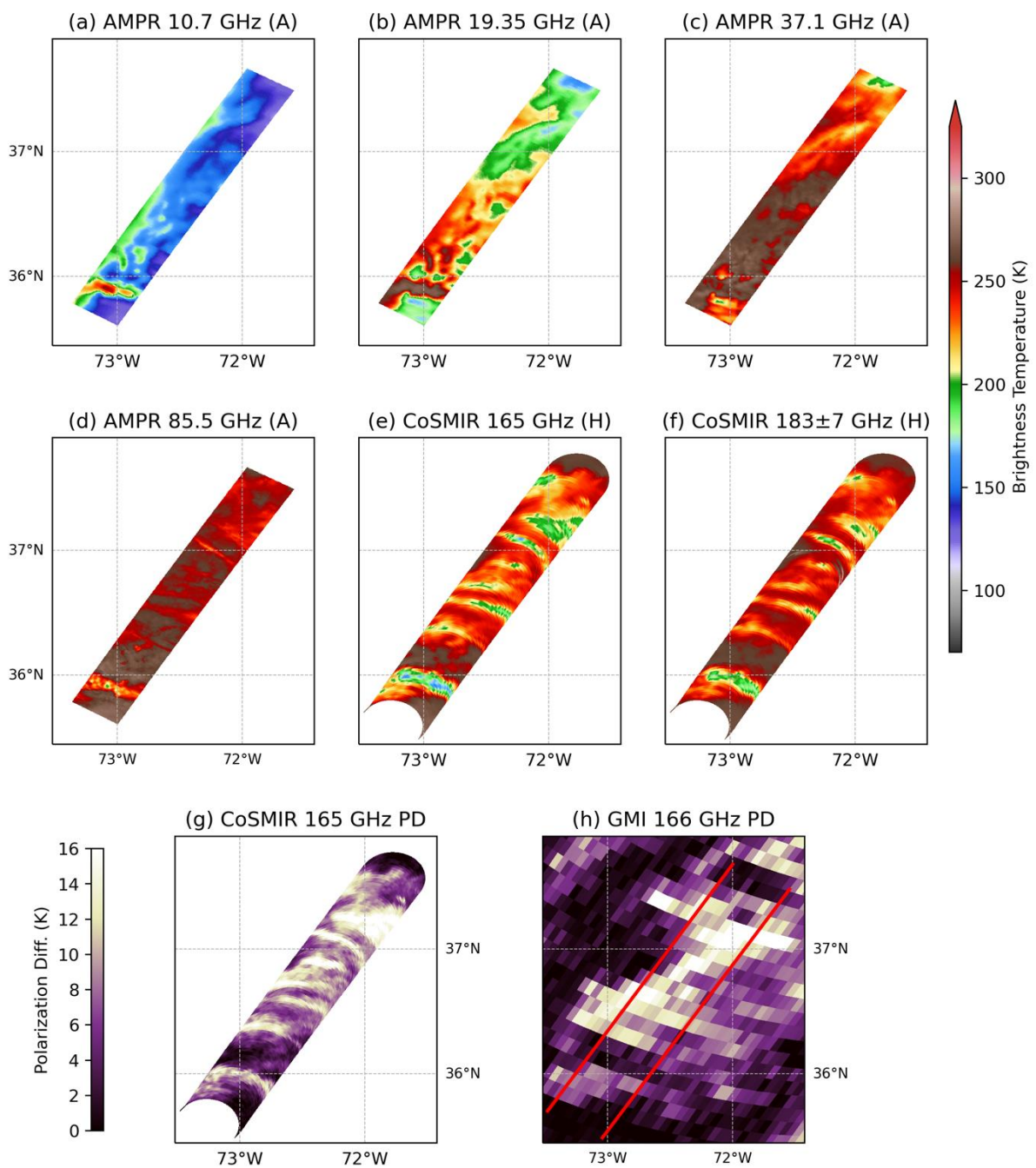
1142

1143 **Figure 13:** Comparison of the (a) HIWRAP and (b) GPM DPR Ku-band reflectivity (dBZ)

1144 during the GPM overpass at 1435 UTC 1 February 2020.

1145

1146



1148

1149 **Figure 14:** AMPR brightness temperatures coinciding with the GPM overpass at 1435 UTC

1150 1 February 2020 at (a) 10.7, (b) 19.35, (c) 37.1, and (d) 85.5 GHz. CoSMIR brightness

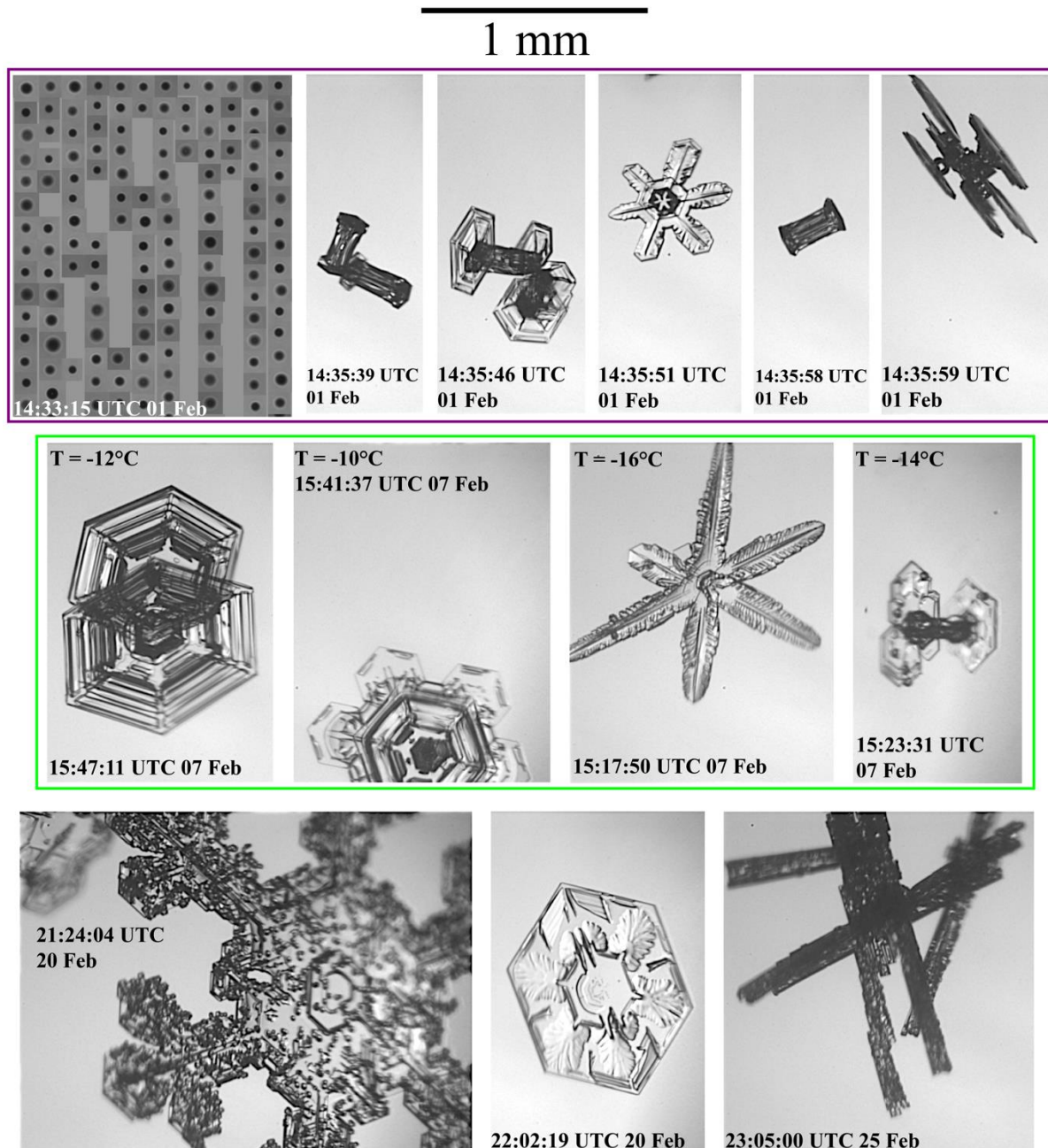
1151 temperatures at (e) 165 GHz and (f) 183 ± 7 GHz. CoSMIR and GMI polarization differences

1152 for the 165 GHz channels are shown in (g) and (h). Red lines in (h) indicate the scan width of

1153 the CoSMIR radiometer. Longitude (x-axis) and Latitude (y-axis) grid lines shown.



Figure S1: Photos from the field. (a) Students launching balloon soundings on Long Island; (b) Forecasters A. DeLaFrance (left), C. Helms (middle) and S. Nicholls (right) preparing a briefing; (c) V. McDonald preparing to board the P-3 for a science flight; (d) G. Sova (left) and K. Sand (right) with PHIPS Instrument PI, M. Schnaiter (middle), on the P-3 between flights. Photo credits: (a) B. Colle, (b) and (d) V. Salazar, (c) V. McDonald taken by J. Finlon.



1163

1164 **Figure S2:** Sample particle images taken by the PHIPS and CPI instruments on the P-3
 1165 during IMPACTS 2020. Times and dates for each image are shown. The images grouped in
 1166 the purple box are from the 1 February case and the images grouped in the green box are
 1167 from the 7 February case arranged so that the images on the left side were from the western
 1168 portions of the flight legs and the images on the right side were from the eastern portions of
 1169 the flight legs.